Universidade de Brasília – Instituto de Geociências (IG)

Programa de Pós-Graduação em Geologia

“MINERALOGIA QUANTITATIVA DE ALTA DEFINIÇÃO E SUA APLICAÇÃO NA EXPLORAÇÃO E PROCESSAMENTO MINERAL - UM ESTUDO DE CASO PARA O DEPÓSITOS DE FERRO N4WS, CARAJÁS-PA”.

VICTOR MOTA E NOGUEIRA

DISSERTAÇÃO DE MESTRADO Nº 459

Orientadora: Prof. Dra. Paola Ferreira Barbosa

Co-Orientadora: Prof. Dra. Adalene Moreira Silva

Brasília - DF

Março de 2020

VICTOR MOTA E NOGUEIRA

“MINERALOGIA QUANTITATIVA DE ALTA DEFINIÇÃO E SUA APLICAÇÃO NA EXPLORAÇÃO E PROCESSAMENTO MINERAL - UM ESTUDO DE CASO PARA O DEPÓSITOS DE FERRO N4WS, CARAJÁS-PA”.

Dissertação apresentada ao Instituto de Geociências da Universidade de Brasília, como requisito para obtenção do grau de Mestre em Geologia.

Orientadora

Profª. Drª. Paola Ferreira Barbosa

Banca Examinadora

Profª. Drª. Paola Ferreira Barbosa

Prof. Dr. Federico Alberto Cuadro Jiménez

Prof. Dr. Leonardo Evangelista Lagoeiro

Brasília, março de 2020.

FICHA CATALOGRÁFICA

Mota e Nogueira, Victor
M? "MINERALOGIA QUANTITATIVA DE ALTA DEFINIÇÃO E SUA APLICAÇÃO NA EXPLORAÇÃO E PROCESSAMENTO MINERAL - UM ESTUDO DE CASO PARA O DEPÓSITOS DE FERRO N4WS, CARAJÁS-PA". / Victor Mota e Nogueira; orientador Paola Ferreira Barbosa; co-orientador Adalene Moreira Silva. -- Brasília, 2020.
65 p.

Dissertação (Mestrado - Mestrado em Geologia) -- Universidade de Brasília, 2020.

1. Mineralogia. 2. Cristalografia. 3. Difração de Elétrons Retroespalhados (EBSD). 4. Transformação de Fase. 5. Martitização. I. Ferreira Barbosa, Paola, orient. II. Moreira Silva, Adalene, co-orient. III. Título.

"When I speak of poetry I am not thinking of it as a genre.

Poetry is an awareness of the world, a particular way of relating to reality."

Andrei Arsenyevich Tarkovsky

AGRADECIMENTOS

Agradeço a minha orientadora Paola Ferreira Barbosa por ter me aceitado como orientando e por me guiar de maneira tão cuidadosa na busca do conhecimento necessário para realizar este trabalho. Agradeço também minhas duas co-orientadoras Adalene Moreira Silva e Catarina Labouré Benfica Toledo que deram todo o suporte necessário para a viabilização da minha pesquisa.

Meus agradecimentos ao CNPq, CAPES e FAP-DF pela concessão de bolsa durante o período de mestrado e apoio financeiro ao trabalho. Agradeço ao Instituto de Geociências, seus professores e funcionários pelo acolhimento desde a graduação e durante todo o mestrado. O presente trabalho foi realizado com apoio da Coordenação de Aperfeiçoamento de Pessoal de Nível Superior - Brasil (CAPES) - Código de Financiamento 001.

Agradeço ao Deutsches GeoForschungsZentrum (GFZ) e Sathish Mayanna pela colaboração e parceria de pesquisa essencial para às análises de microscopia eletrônica e EBSD. Ao professor do Instituto de Física, José Antonio Huamaní Coaquira pelas análises de Espectroscopia Mössbauer e VALE S/A por conceder as amostras.

Agradeço ao meu amigo e seu suporte indispensável durante todos os momentos Fernando Rossi Almeida. Sem sua assistência e fraternidade durante todos estes anos este trabalho não seria o mesmo.

Dedico e agradeço a toda minha família e o suporte dado durante esta jornada, especialmente a Elenise Mota Alves Nogueira, Wagner José Assunção Nogueira, Gustavo Maan, Elaine Mota Alves e Izabela Stephano. A todos meus amigos, colegas e pessoas queridas que me acompanharam durante o mestrado, Robert Beekelaar, Juliana Carvalho, Mariana Machado, Thais Choucair, Vinicius Duarte, Jullie Utsch, Moniélle Martins, Malú Nakamura, Ana Rita Maciel, Maria Masella, Thassio Werlang, Joice Dias e Gustavo Vasconcelos.

LISTA DE ILUSTRAÇÕES

Figure 1: BSE map sections of selected domains for EBSD analysis in Sample A: a) Grain I – magnetite grain exhibiting euhedral triangular habit and hematite transformation along its borders. b) Grain II – trapezoid magnetite grain embedded into magnetie aggragate along the banding, also showing hematite transformation on its edges **9**

Figure 2: Phase map, inverse pole-figure and pole plots of martitized grains composed of magnetite and hematite from Sample A: a) Grain I and b) Grain II..... **10**

Figure 3: BSE map sections of selected domains for EBSD analysis in Sample B: a) Grain III (euhedral hematite grain and magnetite and goethite in its interior) and Grain V (Elongated banding domain containing the three target mineral phases). b) Grain II (hematite grain containining magnetite and goethite on its interior) next to Grain VI (angular grain of hematite embedded into the banding domaing also containing magnetite and goethite on its interior). **12**

Figure 4: Phase map, inverse pole-figure and pole plots of martitized grains containing the three iron oxide phases (magnetite, hematite and goethite) from Sample B: a) Grain II and b) Grain III. **13**

Figure 5: Phase map, inverse pole-figure and pole plots of martitized grains of banding domain containing the three iron oxide/hydroxide phases (magnetite, hematite and goethite) from Sample B: a) Grain III and b) Grain IV..... **14**

Figure 6: Phase map, inverse pole-figure and pole plots of matrix domains of Sample A (a) and Sample B (b)..... **16**

Figure 7: Guide of expected clusters in the misorientation space (cubic-m3m to trigonal-3) for the magnetite-hematite analyses in fundamental zone (Axis-angle). Data is simulated using the orientation relationships from Table 1 and their equivalent ORs in the directions [110] || [11-20], [011] || [11-20] and [01-1] || [10-10]..... **18**

Figure 8: Misorientation distribution of magnetite-hematite boundaries from Sample A and B plotted in the fundamental zone of the axis-angle space. Arrows pointing to clusters related to the direct phase transformation OR-AA' and their equivalents. Sample A: a) Grain I and b) Grain II. Sample B: c) Grain III, d) Grain IV), e) Grain V and f) Grain VI. Clusters are colored and highlighted by their ORs as Figure 7. ..... **20**

Figure 9: a) Guide of expected clusters in the misorientation space (trigonal-3 to orthorhombic-222) for the hematite-goethite phase transition analysis using the ORs from Table II and their equivalent directions; and misorientation distribution of hematite-goethite boundaries from Sample B plotted in the fundamental zone of the axis-angle space, for: b) grain III, c) grain IV, d) grain V and e) grain VI. Arrows pointing to clusters related to the direct phase transformation ORs. **22**

Figure 10: a) Guide of expected clusters in the misorientation space (cubic-m3m to orthorhombic-222; and b) misorientation distribution of magnetite-goethite boundaries from Grain III - Sample B plotted in the fundamental zone of the Axis-Angle space..... **23**

Figure 11: Misorientation distribution of magnetite-magnetite boundaries plotted in axis-angle space with clusters assigned to their CSLs indication (Table III). a) Grain II – Sample A and b) Grain V – Sample B. c) Quality Image Map of Grain II in grayscale showing evidence of lamellar twinning of magnetite. **25**

Figure 12: Misorientation distribution of hematite-hematite boundaries of Grain V – Sample B plotted in axis-angle space with clusters assigned to their twinning plane **27**

Figure 13: Matrix misorientation distribution of magnetite-hematite boundaries from Sample A (a) and Sample B (b) plotted in the fundamental zone of the axis-angle space. Arrows are colored to the assigned cluster and ORs from Figure 7 ..... **28**

Figure 14: Vertical geochemistry analysis of SiO2, MgO, CaO, P2O5, Al2O3 and ASD logging (adapted from Prado et al. 2016) from the drill core F1051 (N4WS), Serra Norte deposit. **32**

Figure 15: Most representative room temperature Mössbauer spectra of the main three lithotypes of the iron ore: A) Ore Canga (OG) – sample F1051-004 B) Friable Hematite sample F1051-078 (FH) and C) Jaspilite (JP) sample F1051-151 ..... **35**

Figure 16: Mössbauer spectra showing the differences between Friable Hematite ores: A) Friable Hematite ore with high hematite and low goethite - sample F1051-020; B) Friable Hematite ore with high hematite and intermediate goethite sample F1051-034. ..... **36**

Figure 17: a) Backscatter image of ore canga sample F1051-12 showing the domains analyzed in the electron microprobe analysis: I – preserved martite crystals with the typical phase transformation texture between hematite and goethite, II – Radial goethite aggregate, III – goethite aggregate. b) Backscatter image of friable hematite sample F1051-46 showing its most common texture of elongated crystals of hematite and transformed goethite. **37**

Figure 18: Projection scheme parallel to [01-1]M modified from Withers & Bursil (1980) exhibiting orientation relationships of Type-A, B, D and S for the quaternary orientationship H/MA/MT/H'/MB proposed, together with the expected correspondents' clusters formed into 3D-misorientation space of Axis-Angle. Note that MT'/H'/MB should be rotated 90o diagonally in order to fit the structure theoretically, but for means of a better visualization in 2D rotation is only indicated. **43**

LISTA DE TABELAS

Table 1: Magnetite-Hematite orientation relationships (Becker et al. 1977 and Whiters & Bursil 1980). n denotes a unit vector that runs parallel to the axis of rotation. **4**

Table 2: Hematite-Goethite orientation relationships. n denotes a unit vector that runs parallel to the axis of rotation. **5**

Table 3: Clustering quantification of the magnetite-hematite grain boundary misorientation analysis. **18**

Table 4: Clustering quantification of the hematite-goethite grain boundary misorientation analysis **22**

Table 5: Coordinates in Rodrigues-Frank space and Axis-Angle of cluster center of theoretical CSL boundaries and the nearest clusters to CSL orientation relationships (for magnetite-magnetite analysis) in Grain II and V. **24**

Table 6: Major elements geochemistry of selected samples of the N4WS - F1051 drill core **30**

Table 7: Average major elements geochemistry of every 20m interval of the N4WS F1051 drill core. **31**

Table 8: Mössbauer Spectrometry Parameters for the N4WS – F1051 ..... **34**

Table 9: Electron microprobe analysis of hematite and goethite by different textures and lithotypes. **38**

LISTA DE ABREVIAÇÕES

BHF	Hyperfine Magnetic Field
BSE	Backscattered Electron
CMP	Carajás Mineral Province
CSL	Coincidence Site Lattice
EBSD	Electron Backscatter Diffraction
EPMA	Electron Probe Micro-Analyzer
FH	Friable Hematite
GHT	Goethite
HEM	Hematite
ICP-AES	Inductively Coupled Plasma of Atomic Emission Spectroscopy
IPF	Inverted Pole Figures
IS	Isomer Shifts
JP	Jaspilite
LWD	Line Width
MAG	Magnetite
MS	Mössbauer Spectrometry
OC	Ore Canga
OR	Orientation Relationships
PF	Pole Figures
QF	Quadrilátero Ferrífero
QS	Quadrupole Splitting
R-F	Rodrigues-Frank

Sumário

I. Introdução i

1.1 Estruturação do volume..... ii

1.2 Objetivos ii

II. Characterization of the crystallographic textures and orientation relationships of the magnetite-hematite-goethite transformation of Archean iron formations from the Carajás Mineral Province, Brazil: case study of topotactic transitions during martitization process in jaspilites from the N4WS deposit..... 1

1. Introduction 2

2. Methods 6

2.1. Sampling..... 6

2.2. BSE Mapping..... 6

2.3. EBSD 6

2.4. Mineral Characterization 7

3. Results 8

3.1. BSE and EBSD observations by IPF and PF..... 8

3.2. EBSD Misorientation Analysis..... 17

3.3. Mineral Characterization of the N4WS Drill core..... 29

4. Discussion..... 40

4.1. Crystallographic Textures and Orientation Relationships 40

4.2. Mineral Characterization 45

***5*. Conclusions 46**

6. References. 48

1. Introdução

A procura por processos cada vez mais eficientes na indústria mineral tem demandado um novo olhar sobre a mineralogia e demais técnicas analíticas aplicadas, desde a etapa de exploração até o processamento e beneficiamento do minério. Para tais técnicas, foi designado o termo *mineralogia de alta definição*, para o estudo quantitativo e automatizado de minerais e rochas aliado a outros recursos tecnológicos e analíticos. As principais técnicas aplicadas na mineralogia de alta definição são aquelas baseadas em um sistema de microscopia eletrônica de varredura, como por exemplo QEMSCAN® e EBSD. A indústria do minério de ferro possui suma importância no cenário mineral brasileiro e tem sido pioneira na introdução de técnicas quantitativas automatizadas. Com a recente entrada de novos equipamentos no mercado brasileiro, torna-se necessário criar uma nova perspectiva, propor novos métodos e criar sistemáticas para o melhor aproveitamento e entendimento do minério de ferro, acompanhando assim as tendências tecnológicas empregadas tanto na indústria global quanto na academia. A mineralogia de processo é considerada como sendo a aplicação prática do conhecimento mineralógico no auxílio da indústria mineral desde as etapas de exploração até a otimização de como o minério pode ser extraído e processado de maneira mais eficiente. A caracterização do minério de ferro e o entendimento dos minerais que o compõem, suas texturas cristalográficas e demais características físico-químicas são fundamentais para o desenvolvimento da mineração e para um melhor entendimento dos processos minerais. As principais técnicas analíticas adjuntas da mineralogia de alta definição que possuem a microscopia eletrônica de varredura (MEV) como plataforma não servem somente para fins de mineralogia quantitativa modal. Os dados gerados também podem ser usados tanto para estudos estruturais e de petrotrama quanto para calibração de informações petrofísicas que alimentam modelos genéticos, por exemplo.

Dados de liberação mineral, textura cristalográfica, orientação preferencial de forma, associação mineral, quantificação de poros, estatística do tamanho das partículas, angularidade, evidências de transformação de fase, estado de oxidação etc, em conjunto, possibilitam a sistematização da caracterização mineralógica de rochas, tornando-a um procedimento quantitativo e passível de comparação entre diversos depósitos minerais (Gottlieb et al., 2000; Sutherland & Gottlieb, 1991; Barbosa & Lagoeiro, 2009; Barbosa et al., 2010; Leiss et al., 2000). Portanto, propõe-se a aplicação dessa sistemática da mineralogia quantitativa de alta definição para os depósitos de ferro N4WS da Província

Carajás como potencial metodologia vinculada ao estudo de processos formadores das (micro)estruturas.

A Província Mineral de Carajás, localizada no setor sudeste do Cráton Amazônico, representa o maior e mais bem preservado setor arqueano do cráton e também possui uma das maiores reservas de ferro do mundo, com aproximadamente 18 bilhões de toneladas de minério de ferro de alto teor (Vasquez et al., 2008; Martins et al., 2017; Gibbs et al., 1986; Machado et al., 1991). O depósito N4WS encontra-se inserido na sequência metavulcanossedimentar Grupo Grão-Pará, que abrange uma área de aproximadamente 18.000 km^2. Esta sequência é atingida por intenso vulcanismo, predominante máfico, atribuído à Formação Parauapebas, sobre- e sotopostas às rochas da Formação Carajás que consistem nos grandes depósitos de ferro de alto teor (média de 65,4% Fe) hospedados em jaspilitos de Carajás (Macambira, 2003). Tanto o minério (hematitito friável) quanto o protominério (jaspilitos), encontram-se metamorfizados em fácies xisto-verde baixo e dispostos em corpos descontínuos (Gibbs et al., 1986; Machado et al., 1991). Serão objetos de estudo fundamental deste projeto os níveis de jaspilitos e minério de ferro do furo de sondagem F1051, pertencentes ao depósito N4WS, que intercepta as zonas mineralizadas em quase sua grande maioria e possui todos os litotipos esperados do minério de ferro.

1.1. Estruturação do volume

Este presente volume de dissertação foi estruturado em duas partes, nas quais contam com uma breve introdução ao tema pesquisado, objetivos e referencial teórico e seguido de uma segunda parte contendo o artigo científico a ser submetido ao periódico *Journal of Applied Crystallography*.

1.2. Objetivos

Este projeto possui como objetivo central reconhecer e caracterizar as microestruturas mais importantes do minério e protominério do depósito N4WS da Formação Carajás. Esse objetivo é alcançado por meio da aplicação de técnicas analíticas avançadas de minerais, contribuindo para o entendimento dos processos de formação de tais estruturas, correlacionando-se dados de texturas cristalográficas, mineralogia modal, química de rocha e transformação de fases. O projeto apresenta uma sistemática de análise

mineralógica que serva, não somente para o minério de ferro de Carajás, mas para qualquer depósito de minério de ferro. Os objetivos específicos são:

i. estudo detalhado da transformação de fase do sistema óxido de ferro;

ii. caracterização textural cristalográfica das principais microestruturas da rocha para investigação de processos de concentração do minério;

iii. sistematização da mineralogia modal ao longo das principais estruturas do depósito, correlacionando-a aos dados de geoquímica total de rocha e assinaturas petrofísicas do minério já disponíveis;

ii. Characterization of the crystallographic textures and orientation relationships of the magnetite-hematite-goethite transformation of Archean iron formations from the Carajás Mineral Province, Brazil: case study of topotactic transitions during martitization process in jaspilites from the N4WS deposit.

Victor Mota e Nogueira[1], Paola Ferreira Barbosa[1], Sathish Mayanna[2, 4], Adalene Moreira Silva[1], Catarina Labouré Bemfica Toledo[1], José Antonio Humaní Coaquira[1], Luciano Mozer de Assis[3].

[1]University of Brasília (UnB) – Institute of Geoscience. Campus Darcy Ribeiro, Brasília, DF, Brazil.
[2]German Research Center for Geosciences (GFZ), Telegradenberg, 14473, Potsdam, Germany.
[3] Vale S.A. - Exploração Mineral de Ferrosos. CTF Miguelão, Fazenda Rio de Peixe, Nova Lima, MG, Brazil.
[4] Carl Zeiss Microscopy GmbH, Carl Zeiss Strasse 22, 73447, Oberkochen, Germany.

Abstract

The most frequent crystallographic textures developed during the progressive phase transformation of magnetite-hematite-goethite are described and analyzed in two natural samples of banded iron formations (jaspilites) from Carajás Mineral Province. Microtextures of martitized grains containing the three phases and the microplaty matrix were analyzed in a scanning electron microscope equipped with a detector for electron backscatter diffraction. For identifying correlation between magnetite, hematite and goethite lattice and topotaxity during transformation, multiple orientation relationship between the three phases were tested and verified also by three-dimensional misorientation spaces. The results show that basal planes of goethite coincide with basal planes of hematite, which coincide with octahedral planes of magnetite. This indicates that the transformation between the three minerals happens topotactically and the oxygen lattice framework is preserved in all members of the reaction as a form of crystallographic memory. As a result of progressive and cyclical changes in oxidation/reduction conditions, an assemblage of high-order orientation relationships is observed and assigned to a complex process of transformation twinning in-between phase transformation of magnetite, hematite and goethite. In the N4WS iron ore deposit of the Carajás Mineral Province, iron oxides/hydroxides from martitized grains work as susceptible markers of environmental changes even still in solid state during the diagenetic process.

1. Introduction

Martitized grains composed of hematite (α-Fe_2O_3, $R\bar{3}c$, a_o=5.038 Å, c_o=13.772 Å), goethite (α-FeOOH, Pnma, a_o=9.945 Å, b_o=3.027 Å, c_o=4.610 Å) and magnetite (Fe_3O_4, $Fd\bar{3}m$, a_o=8.393 Å) are the most common constituents of the iron formations called jaspilite (JP) in the Serra Norte deposits of iron ore in the Carajás Mineral Province (CMP). These jaspilites are precursors of the massive layers of high-grade friable hematite ore. Topotactic phase transformation of the martitization process between magnetite and hematite in iron formations has been extensively described in the Quadrilátero Ferrífero (QF) region in Brazil by electron backscatter diffraction technique (EBSD), but there is a lack of data of quantitative crystallographic textures, phase transformations and mineral characterization within the jaspilites from CMP.

The complete natural phase transformation between magnetite-hematite-goethite and its orientation relationships (ORs) has not been described in detail in the literature for natural cases and still not very understood, but its pairs (magnetite-hematite and hematite-goethite phase transitions) are known for being well described processes in both natural and synthetic samples and for containing systematic coincidences during transitioning processes. During progressive oxidation and reduction of iron oxides/hydroxides, the cubic, trigonal and orthorhombic lattices of the three minerals are linked by specific topotactic relations related to the oxygen lattice framework, being the hematite, in most cases, the intermediate phase in natural systems. In CMP and in many high-grade iron ore deposits around the world, goethite plays a very important role as the final phase in the transformation process and being a substantial part of the bulk high-grade ore and should be considered in the topotactic transformation chain of natural iron oxides/hydroxides.

The samples analyzed in this study come from the jaspilite and iron ore sequence of the N4WS deposit from the CMP that shows very preserved sequences of undeformed jaspilite, friable high-grade ore and mineral canga. The two samples for crystallographic characterization of the textures represent the two extreme stages in the phase transformation process in the target rock (jaspilite). For the EBSD analysis, the first and deepest sample contains the early transformation relation between magnetite and hematite. The second sample is closer to the high-grade ore layers, where the three phases coexist inside the same grain with textural evidences of direct transformation. For

comparison purposes, not only grain analysis was done, but in both samples, the jasper/quartz and microplaty hematite matrix, which compose the primary banding of the iron formation, were also analyzed.

The natural transformation process between magnetite, hematite and goethite occurs due to different stabilities in oxidizing domains, whereas in aqueous systems, the stability Eh/pH diagram indicates magnetite in a very restricted alkaline and reducing field, and hematite is stable in a much wider pH range and fO_2. Stability diagrams consistently show the pair magnetite-hematite, but depending on the data used, the goethite can replace hematite in the diagram and be part of the $Fe\text{-}O_2\text{-}H_2O$ system, or metastable phases as maghemite or other FeOOH polymorphs (Cornwell & Schwertmann, 2003). The stability field of goethite broadens as P_{H2O} increases (Cornwell & Schwertmann, 2003), which is in conformity with the samples analyzed.

In most cases in which iron oxide's topotactic phase transformations were analyzed in iron formations by EBSD technique, orientation relationships have been the most used parameter for describing the crystallographic textures and the relationship between the oxide/hydroxide phases. Those studies used a simple model of finding coincidental maximas in pole figures (PF) and analyzing inverted pole figures (IPF) in order to describe the parallelism between crystallographic orientations. But to consider only orientation in the phase transformation analysis is now consider to be a significant loss of information regarding the crystallographic relationships between crystals (Krakow et al. 2017), and with a complex phase in the system, as goethite, statistics through pole figures, showing only orientation planes of low-index crystallographic planes are not enough to describe the transformation process and the necessary rotation angle of misorientation.

Orientation is defined as a passive rotation expressed in coordinates from a crystal reference into a specimen reference system (Krakow et al. 2017), whereas orientation information of only one crystal specimen is analyzed. Misorientation can be defined as the difference of orientation between two crystallites and it is also a passive rotation in 3D space, but in this case, between two crystal references frames, where both orientations are considered and an orientation relationship between two phases could be better described (He et al. 2004 & Krakow et al. 2017). The grain boundaries can be expressed as a rotation about a common axis to both crystal frames and this kind of misorientation data, called angle-axis pair description can be better visualized into a three-dimensional

space using Rodrigues-Frank (R-F) vectors (He et al. 2004) or Axis-Angle, and in this case the domain used would be restricted to only the coincidental fundamental zone between the two phases selected (Krakow et al. 2017). This new technique for modeling and visualizing misorientaion for topotactic transformation of natural iron oxides and hydroxides samples, could lead into a better understanding and characterizing of crystallographic relationships between the phases, with the graphic visualization of rotational angles of misorientation necessary for the theoretical parallelism between the phases with low- and high-index crystallographic planes. This technique can also show how much the phase transformations contribute to the bulk texture of the analyzed grain/rock and how those transformations between oxides and hydroxides are related to important textures in banded iron formations and iron ores in general. In this study, both orientation and misorientation data were considered and used for describing the main crystallographic textures and relationship between crystals.

For this study, not only the most common topotactic orientation relationship for the magnetite-hematite is considered, described in Heizmann (1981) and Becker *et al.* (1977) (OR A - Table 1). High-index orientation relationships have been also described for natural and synthetic samples of hematite when submitted to different and cyclical conditions of temperature and reduction experiments (OR B, C and D – Table 1). These OR are described in Becker *et al*., (1977) and Whiters & Bursill (1980) and were also considered in this study during 3D misorientation analysis.

Those secondary high-index relationships are not necessarily topotactic as they are a result of what is defined by Whiters & Bursill (1980) as magnetite and hematite transformation twinning followed by new generations of recrystallized magnetite and hematite, generating a complex and diverse system of orientation relationships as OR S (Table 1). For a better quantification of those OR, other equivalent OR in different directions were also considered and analyzed, followed by a briefly analysis of twinning within the samples for magnetite and hematite.

Table 1: Magnetite-Hematite orientation relationships (Becker et al. 1977 and Whiters & Bursil 1980). n denotes a unit vector that runs parallel to the axis of rotation**.**

OR	Parallelism	Axis-Angle
(A)	$(111)_{Mag} \parallel (0001)_{Hem}$, $[110]_{Mag} \parallel [10\text{-}10]_{Hem}$	**n**, 54.74°
(B)	$(112)_{Mag} \parallel (0001)_{Hem}$, $[110]_{Mag} \parallel [10\text{-}10]_{Hem}$	**n**, 35.26°
(C)	$(113)_{Mag} \parallel (0001)_{Hem}$, $[110]_{Mag} \parallel [10\text{-}10]_{Hem}$	**n**, 25.24°

(D)	$(115)_{Mag} \parallel (0001)_{Hem}$, $[110]_{Mag} \parallel [10\text{-}10]_{Hem}$	**n**, 15.69°
(S)	$(111)_{Mag} \parallel (10\text{-}10)_{Hem}$, $[11\text{-}1]_{Mag} \parallel [11\text{-}20]_{Hem}$	**n**, 45.00°

Table 2: Hematite-Goethite orientation relationships. n denotes a unit vector that runs parallel to the axis of rotation.

OR	Parallelism	Axis-Angle
(α)	$(0001)_{Hem} \parallel (001)_{Ght}$, $[11\text{-}20]_{Hem} \parallel [100]_{Ght}$	**n**, 0.00°
(β)	$(0001)_{Hem} \parallel (001)_{Ght}$, $[0\text{-}110]_{Hem} \parallel [100]_{Ght}$	**n**, 30.00°

For orientation relationships regarding the transformation stage of hematite to goethite, the expected ORs can be seen in Table 2. According to Cudennec & Lecerf (2005), both goethite and hematite can be defined as a distorted hexagonal close packing, whereas goethite has half of its sites filled and hematite two thirds of it. Along goethite structure, the anions are stacked perpendicular to c-axis (ABA stacking), just as the hematite structure which is also stacked along c-axis but with minor anions and cations changes. Those minor changes result in the elongation of hematite axis and the distance between ABA arrange, but during the transformation there are not many changes in the cubic packing structure of both minerals (Cudennec & Lecerf, 2005), which indicates that the most reasonable OR expected would be between the parallelism of basal planes $(0001)_{Hem}$ and $(001)_{Ght}$, with OR α representing the $[10\text{-}10]_{Hem} \parallel [100]_{Ght}$ direction and OR β the $[11\text{-}20]_{Hem} \parallel [100]_{Ght}$.

The main objectives of this study are to describe the most frequent crystallographic textures developed during the progressive phase transformation of magnetite to hematite and hematite to goethite and to verify if it is possible to establish a genetic relationship between the phases and if transformation leaves a crystallographic memory until its last member. After the crystallographic textures are described, it is also an objective to verify if the textures here identified can be correlated with chemical and other physical data obtained by other analytical techniques. This might be useful for evaluating the extent to which the crystallographic orientation of magnetite, hematite and goethite can be attributed to phase transitions. We expect to contribute to the debate of the diagenetic process in jaspilite in Archean banded iron formations and how iron oxides and hydroxides can carry important information regarding environmental changes during geological time due to its easily reactivity and transitioning character.

2. Methods

2.1. Sampling for EBSD analysis

Samples were collected from a 355 meters' deep drill core (F-1051) from the deposit N4WS provided by the company VALE S.A. This specific drill core was chosen by its low deformation, almost absence of volcanic intrusions in iron formations and a complete sequence of jaspilites, high-grade friable ore and mineral canga. For EBSD analysis, only the jaspilite portion was chosen. The two extremes of it was selected: Sample A (300 m to 302 m deep) containing euhedral magnetite crystals and early stage phase transition to hematite and Sample B (200 m to 202 m deep) containing grains with the three existing phases and a higher degree of phase transformation and mineral banding. Both samples represent the bottom and the top, respectively, of the preserved jaspilite sequence: Sample A is adjacent to the volcanic rocks that underlay the sequence and Sample B is closer to the high-grade ore. The two thin sections for EBSD analysis were polished in colloidal silica for seven hours in a vibratory polisher.

2.2 *BSE Mapping*

Prior to the main analysis, backscattered electron (BSE) maps of the whole thin sections were carried out on a Zeiss Gemini Column Ultra Plus Field Emission-Scanning Electron Microscope of the Potsdam Imaging and Spectral Analysis (PISA) Facility at the German Research Centre for Geosciences (GFZ) and the appropriate grains were selected for EBSD analysis. Grains from Sample A containing magnetite and hematite indicating phase transformation were selected and grains with the three target phases (magnetite, hematite and goethite) in Sample B were selected. The samples were carbon coated and analyzed with an accelerating voltage of 20kV, working distance of 9 mm and an aperture size of 120 μm, and beam current of 4.0 nA

2.2. *EBSD*

Thin sections were final polished using 0.02 nm silicon colloids, EBSD measurements were carried out at a low vacuum of ~ 100 mbar on a FEI Quanta 3D Dual Beam FEG equipped with an EDAX electron backscatter diffraction system at PISA

facility of the GFZ. Data acquisitions were made by the EDAX TEAM software, where Kikuchi patterns were well selected for each phase according to its crystal system. Data analyses were done using Channel 5.0. MTEX (Hielscher & Schaeben, 2011; for three-dimensional misorientation spaces study, graphics were generated according to the study of Krakow et al. (2017). An accelerating voltage of 20 kV, beam current of 4.0 nA and working distance of ~15 mm were used for the EBSD analysis. The samples were not carbon coated. The SEM stage was controlled manually to the selected areas in BSE mapping and forescattering electron images were generated to each area. Phase maps and orientation maps (inverse pole figure maps) were generated using Tango software and pole figures generated with Mambo Software using contouring calculation of the clustering poles. Phase maps were colored in the following colors: blue for magnetite, red for hematite and yellow for goethite. Three-dimensional misorientation spaces were generated on MTEX software (Hielscher & Schaeben, 2011; Krakow et al., 2017) combining fundamental zones of two selected analyzed phases. The experimental misorientation data was plotted and compared to the computer experimental misorientation clusters showing space-geometrical correlation between faces and crystallographic directions between two coincident crystals.

2.3. Mineral Characterization

After the crystallographic textures are identified and the phase transformation process of iron oxides in the area is better understood, a more complete mineral classification of the drill core was done in order to identify the spatial distribution of iron (hydro)oxides in Carajás Iron Ore from the N4WS deposit, recognizing if the different textures of the ore are a significant factor to correlate chemical and petrophysical data. A different sampling process is proposed for each technique.

The characterization of the ore using semi-quantitative methods of reflectance spectroradiometry and other petrophysical studies (Ferreira, 2015 and Prado et al. 2016) was already done and with them it was possible to identify the main lithotypes of the ore and even subdivide them into other more specific categories regarding their mineral composition (Fig. 1). This study also aims, with the use of ^{57}Fe Mössbauer Spectrometry, Electron Probe Micro-Analyzer and geochemistry obtained by ICP-AES to identify and characterize the iron ore of the N4WS deposit by the study of other samples of the drill core F1051, which contains the main lithotypes of the iron ore of the deposit.

^{57}Fe Mössbauer spectrometry (MS) analysis measurements were done at room temperature of 300K using transmission mode and in a constant acceleration spectrometer with a triangular waveform using a 57Co/Rh source. The isomer shifts quoted in this analysis are relative to the value of α-Fe thin film. Samples for the Mössbauer Spectrometry were selected every 30 meters in the same drill core section and amples were crushed manually.

The MS spectra were analyzed and interpreted based on the resulting parameters and the relative abundance of each phase was calculated based on the area of the sextets and duplets which corresponds to Fe-rich phases in the ore, resulting in a mineral characterization of the main lithotype levels of the iron ore and also the protore: the ore "canga" (OC), friable hematite (FH) and jaspilite (JP).

Inductively coupled plasma of atomic emission spectroscopy (ICP-AES) analyses of major elements were also done for the same drill core but every 2 meters and punctual mineral chemistry analyses of iron oxides/hydroxides were made by Electron Probe Micro-Analyzer (EPMA) in a JXA-8230 – JEOL in the Laboratory of Electron Microscopy of the Institute of Geoscience – University of Brasília. For electron microprobe analysis, samples containing the target textures from each rock type were chosen. The analytical conditions were 15 kV, 20nA beam current and counting time of 10s in the peak of characteristic lines and 5s in each background.

3. Results

3.1. BSE and EBSD observations by IPF and PF.

3.1.1. Sample A

In this first analyzed sample, the microstructural and crystallographic aspects of phase transition between magnetite and hematite show evidence of initial stage of transformation. This sample belongs to the interval between 300 m to 302 m deep of the drill core sampled for this study. The grains are mainly composed of magnetite and hematite along its border or in its interior (darker gray contrast in BSE images - Fig. 1). Grains are usually shrouded by micro-platy hematite and chert matrix or embedded into banded aggregates domains. In both domains, grains are squared and tabular, most of times well-developed in size when compared to the small size of crystals in the matrix. One grain of each domain, displaying direct phase transformation along their octahedral

planes, was chosen and is shown in Figure 2. Those straight swaddle bands are a strong indication of crystallographic control of transformation (Davis 1968, Barbosa & Lagoeiro 2009) and can be easily seen in both phase maps of Figure 2, in conventional BSE-SEM images or in optical microscopy.

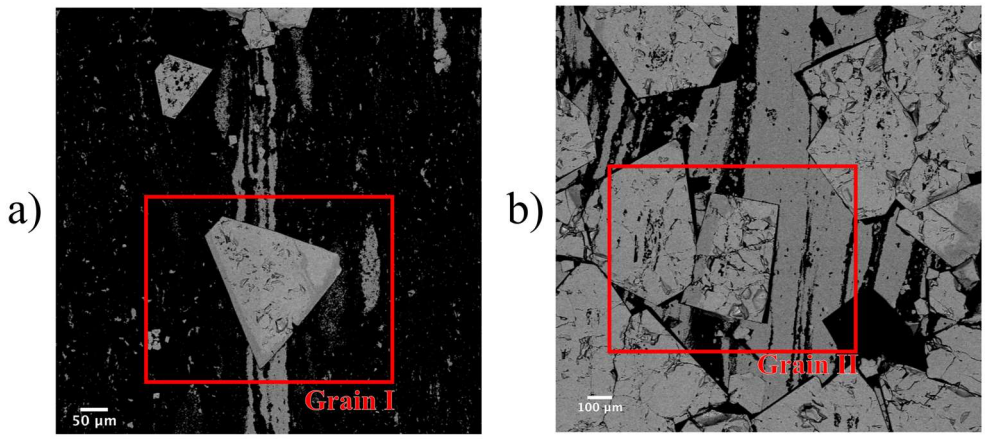

Figure 1: BSE map sections of selected domains for EBSD analysis in Sample A: a) Grain I – euhedral magnetite grain and hematite along its borders. b) Grain II – euhedral magnetite grain embedded into magnetie aggregate along the banding, also showing hematite on its boundaries.

Magnetite is displayed in blue and hematite in red in Figure 2. The first grain described, Grain I of Sample A, is a triangular shaped grain (ca. 200 µm of diameter) mostly composed of magnetite (74%) with straight layers of hematite (39%) along its border (ca. 15µm of diameter) or crossing the interior of the crystal. This grain is embedded by matrix and crosscuts the primary banding of the rock. Grain II of Sample A, differently, is surrounded by an aggregate of magnetite crystals following banding of the rock. Grain II is euhedral with a dimension of 130 x 200 µm. It has hematite layers along its edges and a tabular hematite of 25 µm in its interior. This grain is composed of magnetite (61%) and hematite (39%).

Inverse pole figure maps of both grains are also shown in Figure 2 for a better visualization of spatial orientation of magnetite and hematite lattice. Inverse pole figure maps show direct correspondence between the grains mean orientation and assigned colors. In both crystal systems of magnetite and hematite, the octahedral (111) and basal (0001) planes normal are fixed along the Z-direction. Magnetite crystals show a single preferred orientation represented by a lime green color in Grain I and light green in Grain II. Hematite in Grain I is marked by straight stripes showing one single orientation.

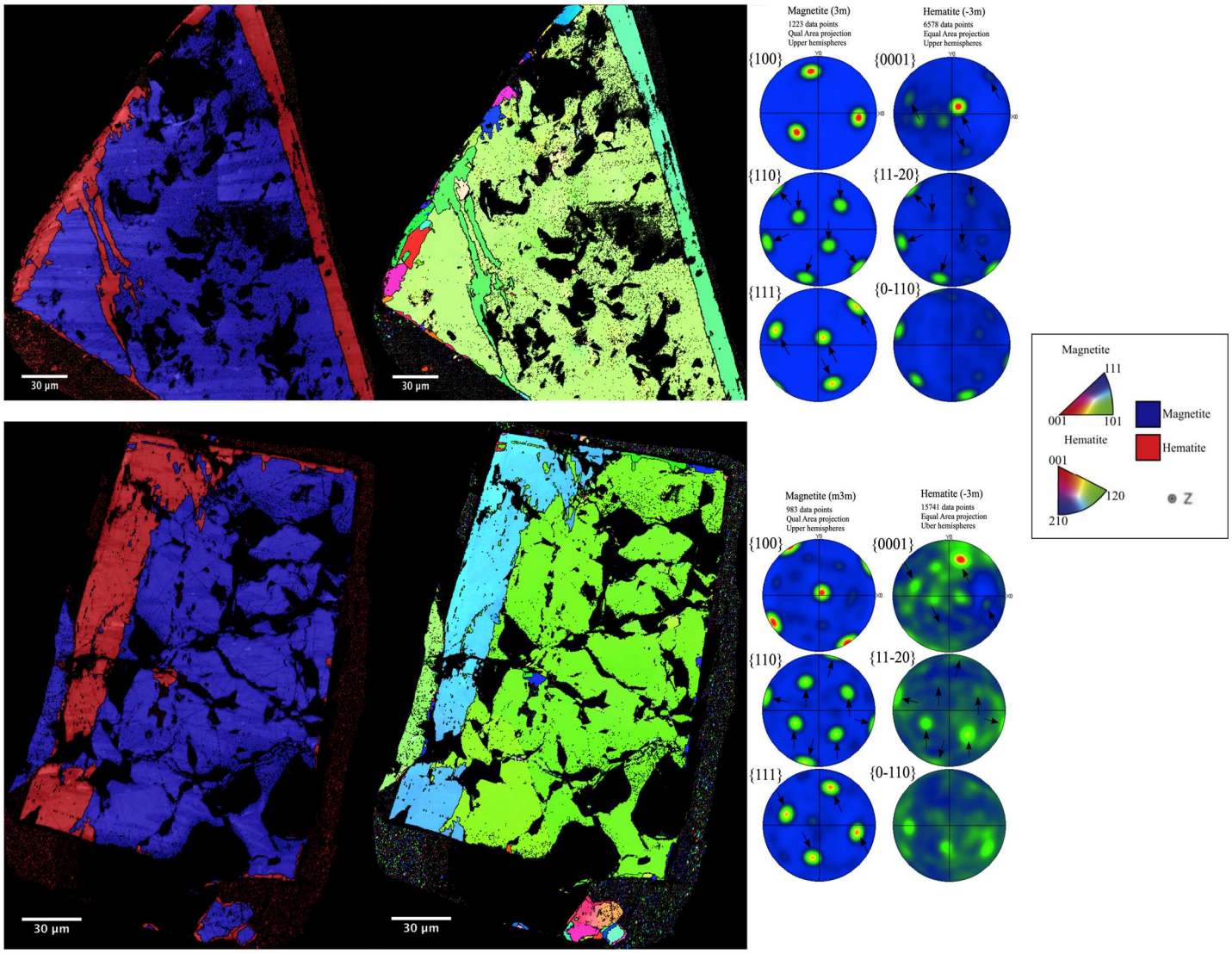

Figure 2: Phase map, inverse pole-figure and pole plots of martitized grains composed of magnetite and hematite from Sample A: a) Grain I and b) Grain II.

Poles figures relative to the [100], [110] and [111] directions were generated for magnetite and [0001], [11-20], [0-110] for hematite (Fig. 2). In both grains, the poles of octahedral (111), dodecahedral (110) and hexahedral (100) planes are very concentrated, which indicates a preferred orientation of the orientation of a single crystal. The poles of octahedral (111) and dodecahedral (110) planes for Grain I show 4 and 7 maximas, respectively, which are coincident with the basal (0001) and prismatic (11-20) planes pole figures of hematite (marked by black arrows). In pole figures of Grain II, 4 and 8 maximas can be seen in the poles figures relatively to octahedral (111) and dodecahedral (110) planes, respectively. They coincide with pole figures of hematite of (0001) and (11-20) planes.

3.1.2. Sample B

In this second analyzed sample (Fig. 3), the three iron minerals of this study are in contact. The microstructural and crystallographic aspects of magnetite, hematite and goethite show evidence of an advanced stage of transformation. The three phases are easily distinguishable in backscatter images. This sample belongs to the interval between 200 m to 202 m deep of the drill core sampled for this study. The grains are mainly composed of hematite displaying inner domains with smaller grains of magnetite and goethite. As in the previous sample, grains can be shrouded by micro-platy and chert matrix or embedded into banded aggregates domains. In both domains, martitized grains display hexagonal and rhombic euhedral shapes and tabular hematite is parallel to the banding of the rock. Two areas of each domain (Fig. 3), displaying direct phase transformation were chosen and are shown in Figure 4, for the single grains domains, and Figure 5**,** for aggregate domains.

Grain III from Sample B has a hexagonal shape (ca. 100 x 75 μm in size, of larger and smallest diameter) composed of 43% of hematite, 34% of magnetite and 23% of goethite (Fig. 4a). This grain is shrouded by matrix and partially filled with smaller grains of magnetite and goethite. Near the grain edges, it is also possible to see layers of goethite, indicating either the direct transformation between hematite and goethite or the precipitation of goethite. Grain IV from Sample B (Fig. 4b) shows the same features as the previous grain with an approximately size of 100 x 85 μm of diameter and it is composed predominantly by 62% of hematite, 21% of magnetite and 17% of goethite.

Pole figures relative to the directions [100], [110] and [111] were generated for magnetite; [0001], [11-20], [0-110] for hematite and [100], [010] and [001] for goethite (Fig. 4). In both grains III and IV, the octahedral (111), dodecahedral (110) and hexahedron (100) pole planes distribution for magnetite are very concentrated, which

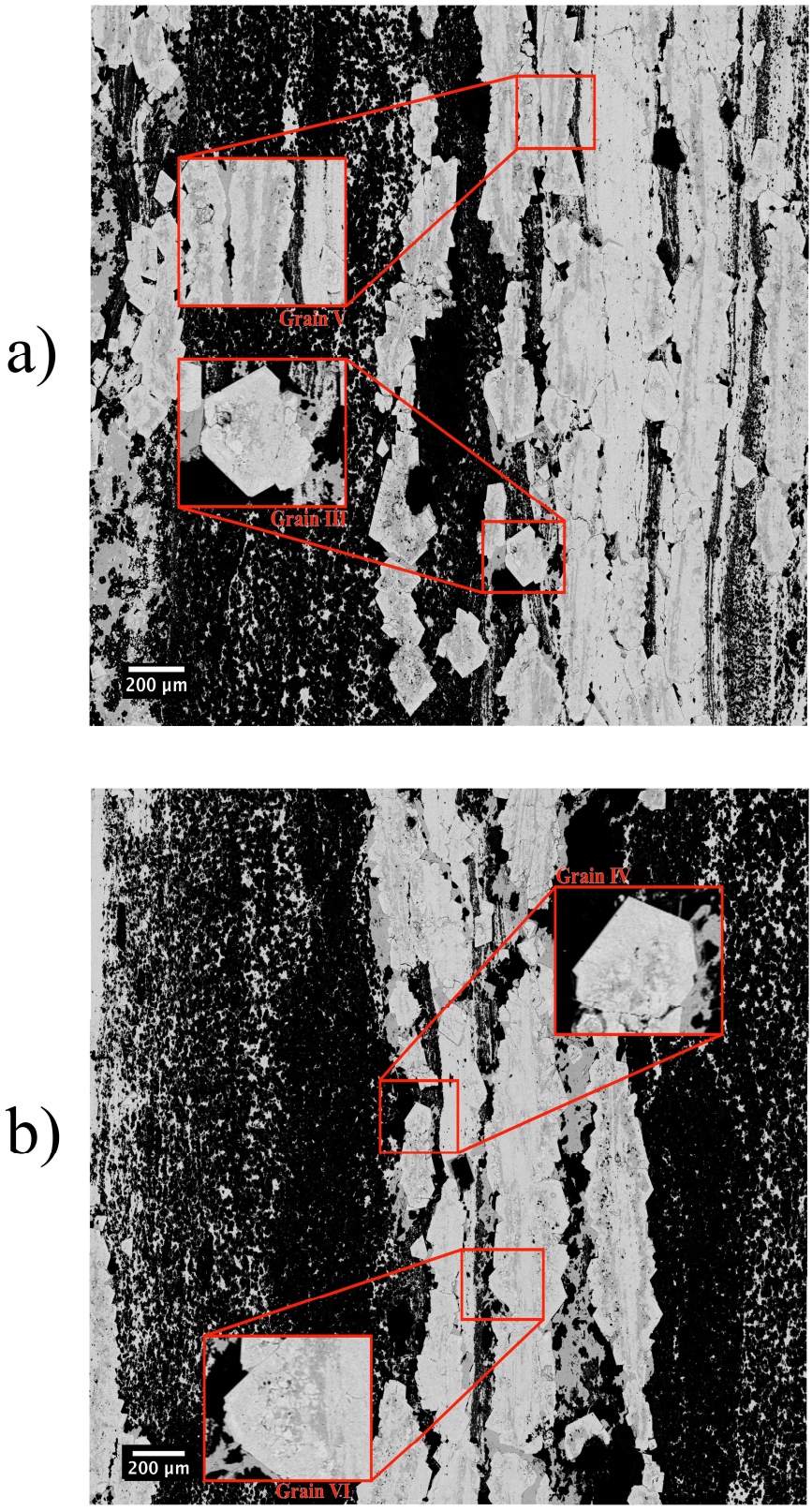

Figure 3: BSE map sections of selected domains for EBSD analysis in Sample B: a) Grain III (euhedral hematite grain and magnetite and goethite in its interior) and Grain V (Elongated banding domain containing the three target mineral phases). b) Grain IV (hematite grain containining magnetite and goethite on its interior) next to Grain VI (angular grain of hematite embedded into the banding domaing also containing magnetite and goethite on its interior).

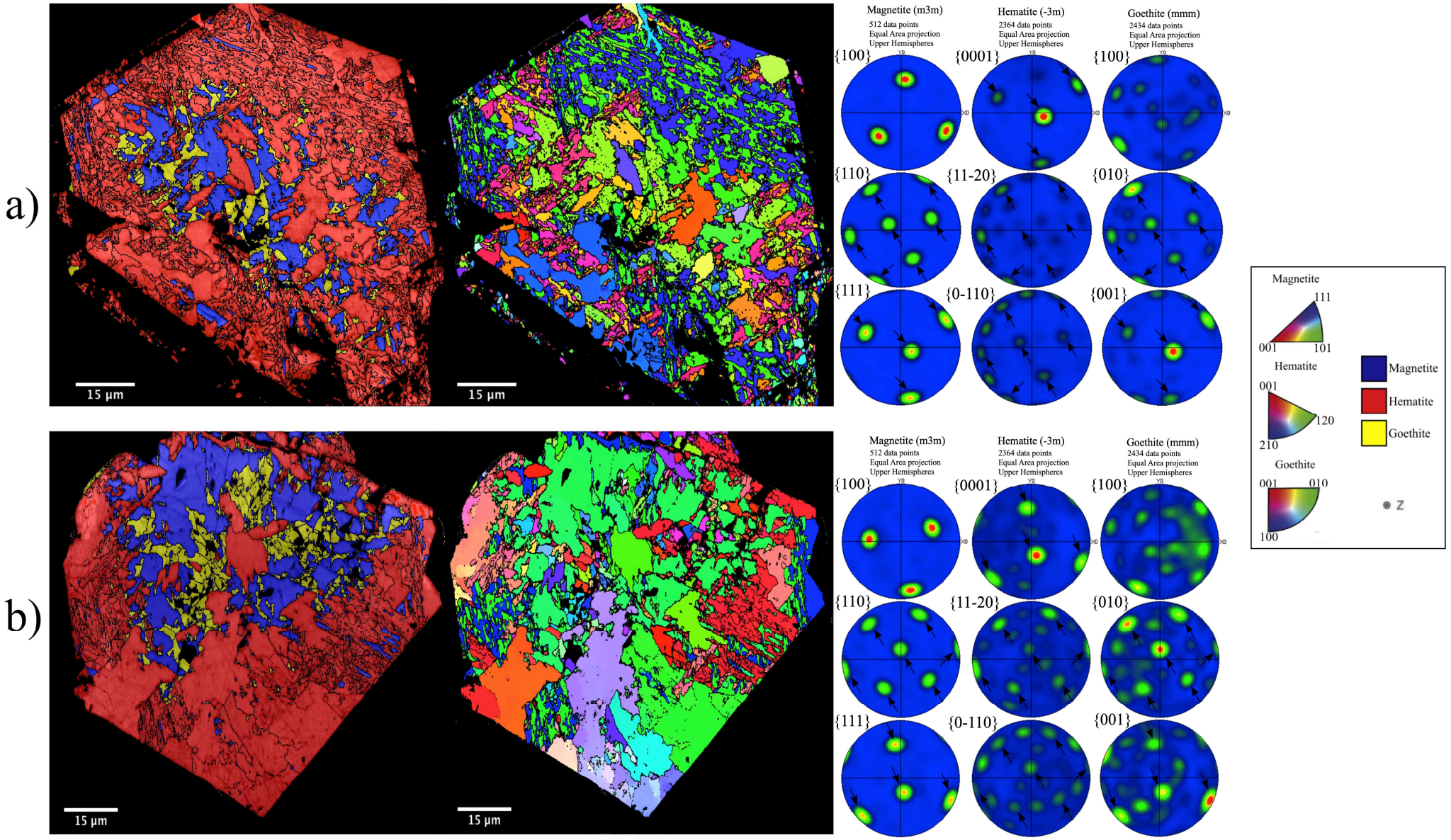

Figure 4: Phase map, inverse pole-figure and pole plots of martitized grains containing the three iron oxides/hydroxides phases (magnetite, hematite and goethite) from Sample B: a) Grain III and b) Grain IV.

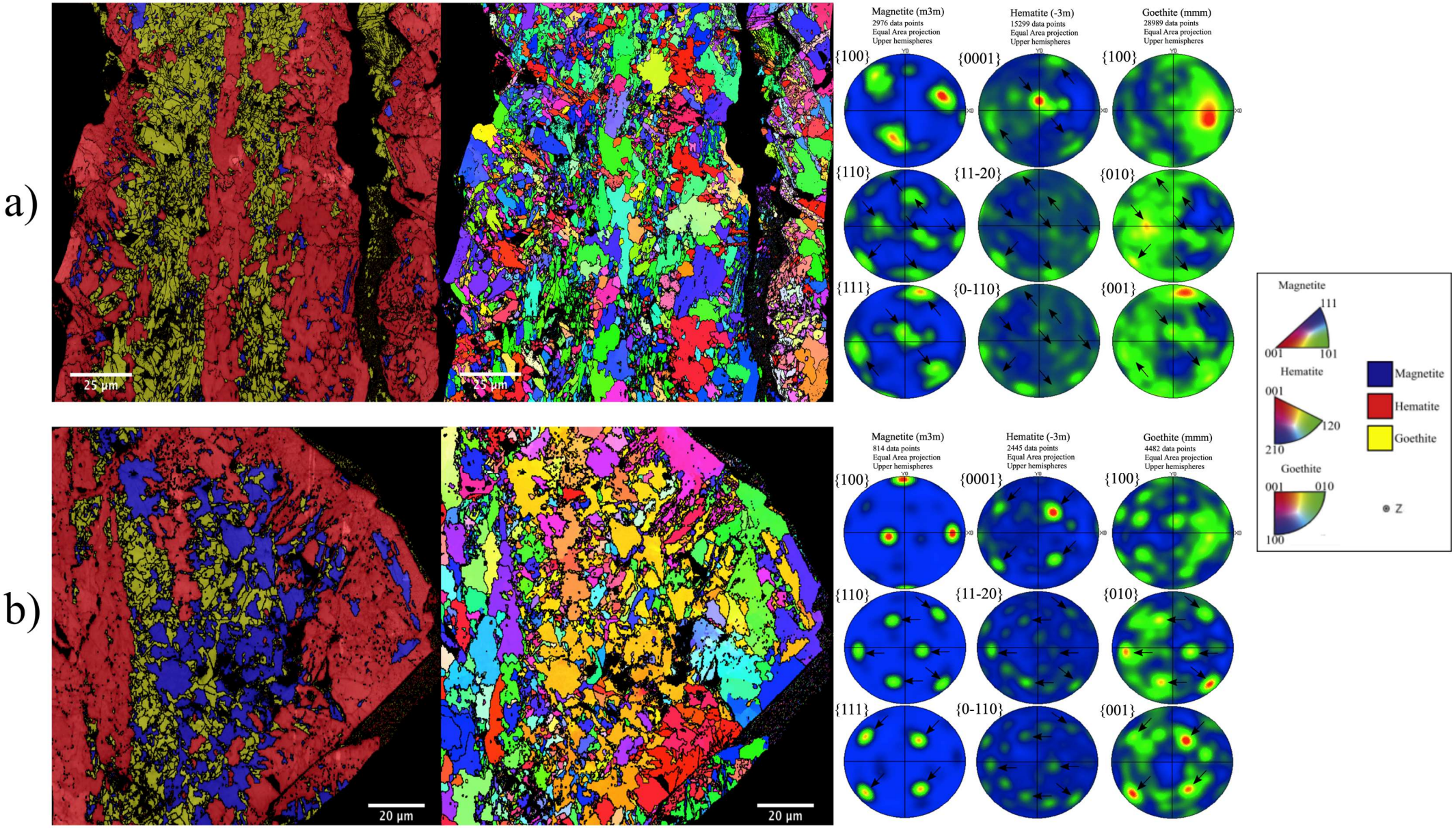

Figure 5: Phase map, inverse pole-figure and pole plots of martitized grains of banding domain containing the three iron phases (magnetite, hematite and goethite) from Sample B: a) Grain V and b) Grain VI.

indicates a single crystal orientation. Pole figures of octahedral (111) and dodecahedral (110) planes for Grain III and IV show 4 and 7 maximas, respectively, which are coincident with the basal (0001) and prismatic (10-10) / (11-20) planes poles of hematite and with the basal (001) and prismatic (010) planes poles of goethite (marked by black arrows in Fig. 4).

In Figure 5 we see Grain V and VI from Sample B. Grain V is in fact a section of tabular hematite (ca. 100 μm width) composed primarily of 54% of hematite, 22% of magnetite and 24% of goethite (Fig. 5a). This grain is part of a bigger banding domain mostly composed of hematite and goethite along the banding. Magnetite is present as sparse smaller grains in both hematite and goethite domains. Grain VI from Sample B (Fig. 5b) shows similar characteristics to grains from Figure 2 (ca. 120 μm in diameter) and it is composed of 54% of hematite, 22% of magnetite and 24% of goethite.

The pole figures of Grain V show a more scattered orientation for the three phases, when compared to grain PF presented before, whereas in Grain VI magnetite and hematite pole figures maximas are more concentrated. Octahedral (111) and dodecahedral (110) planes' pole figures for Grain V shows 4 and 7 maximas while Grain VI show 4 and 6 maximas, respectively, which are coincident with the basal (0001) and prismatic (10-10) / (11-20) planes pole figures of hematite and with the basal (001) and prismatic (010) planes pole figures of goethite. Goethite in both samples exhibits quite scattered pole figures when compared to the previous grains from Sample B, even though the maximas are still easily recognizable in the pole figures.

3.1.3. Matrix A and B

Phase Maps, Inverted Pole Figures and Pole Figures were generated for domains containing only the matrix of both samples (Fig. 6). The matrix is predominantly composed of microplaty hematite (Sample A: 94% of hematite, 6% of magnetite; Sample B: 64% of hematite, 1% of magnetite, 35% of goethite); crystallographically distinct from the previously analyzed grains of martite, the pole figures for the matrix of Sample A and Sample B show a preferential orientation of planes, seen mainly by the concentration of points in the Y-direction of the pole figure (0001)Hem and (001)Ght and also by a cluster of points along the X-axis of (11-20)Hem and (0-110)Hem pole figures.

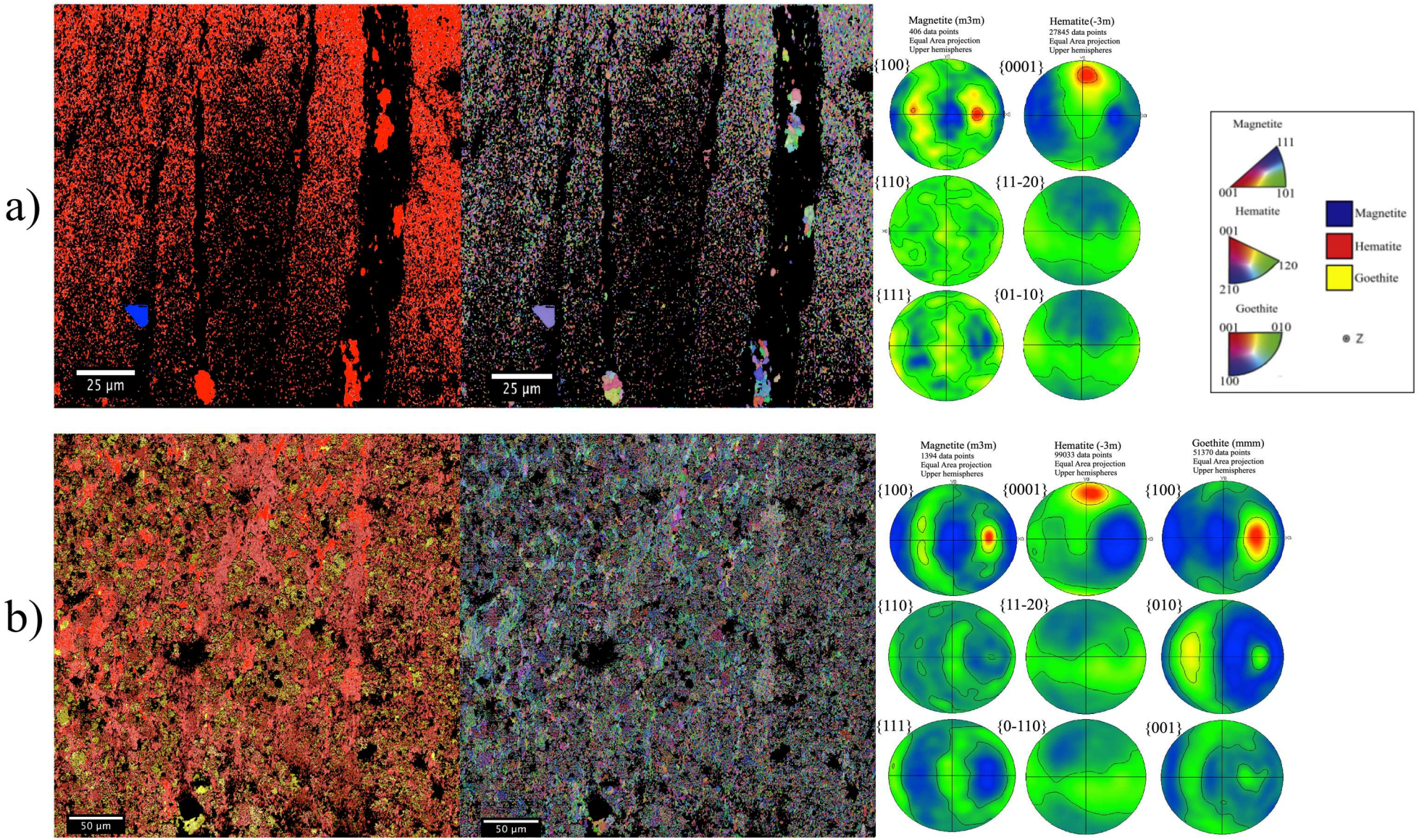

Figure 6: Phase map, inverse pole-figure and pole plots of matrix domains of Sample A (a) and Sample B (b).

3.2. EBSD Misorientation Analysis

3.2.1. Magnetite-hematite orientation relationships

For a better understanding of the expected crystallographic relationships between magnetite and hematite and their rotation centers, a visual guide of clusters was simulated relatively to each OR from Table 1 and their equivalent directions in the appropriate fundamental zone (Fig. 7). Here we call Type-A orientation relationships those with low-index crystallographic planes $(111)_{Mag}||(0001)_{Hem}$ in all equivalent directions of $<110>_{Mag}$ || $<10\text{-}10>_{Hem}$, Type B-D those with high-index crystallographic planes $(11l)_{Mag}||(0001)_{Hem}$ with $l>2$ and Type S those with $(111)_{Mag}$ || $(10\text{-}10)_{Hem}$ or $(111)_{Mag}$ || $(11\text{-}20)_{Hem}$. The rotation centers of each cluster in Figure 7 were used to color and highlight the ORs which this study aims. The first domain refers to the ORs cited in Table 1 (clusters A to D, Fig. 7). They share the same direction $[110]_{Mag}$ || $[10\text{-}10]_{Hem}$ and have a rotation angle respectively of ~54.74°, ~35.26°, ~25.24° and ~15.79°. The clusters move towards the center of the fundamental zone as their crystallographic index *l* of the OR increases. The same angularity can be observed in the directions $[110]_{Mag}$ || $[11\text{-}20]_{Hem}$ and $[011]_{Mag}$ || $[11\text{-}20]_{Hem}$ as they are equivalent clusters of those previously mentioned here. The clusters found in the edges of the fundamental zone (Type-A) are assigned to the most expected topotactic orientation relationship between magnetite-hematite transition. The clusters S and S' (Type-S) formed at the side of the fundamental zone and with rotational angle of ~45° are an expected coincidence which is consequence of Type-B ORs (Whiters & Bursill, 1980), but not usually seen in previous studies or in pole figures. A table with all orientation relationships misorientation clusters of grains, their misorientation statistics and variations in a 5º radius is presented in Table 3.

Crystallographic relationships between grain boundaries domains of magnetite-hematite inside martitized grains were assessed by plotting misorientation within the corresponding fundamental zone of the Axis-Angle space (Fig. 8). Boundary misorientations are clustered near a ~54.74°, ~35.26°, ~25.24° and ~15.79° rotation about the $[110]_{Mag}$ || $[10\text{-}10]_{Hem}$ axis and the perpendicular directions $[110]_{Mag}$ || $[11\text{-}20]_{Hem}$ and $[011]_{Mag}$ || $[11\text{-}20]_{Hem}$ and also near a ~45° rotation about the $[11\text{-}1]_{Mag}$ || $[11\text{-}20]_{Hem}$ and $[11\text{-}1]_{Mag}$ || $[10\text{-}10]_{Hem}$. Grain I from the sample A (Fig. 8a) shows pronounced clustering in ORs of Type A. Orientation relationships of Type-A show the highest density of points among all of them, especially in the direction $[011]_{Mag}$ || $[11\text{-}20]_{Hem}$.

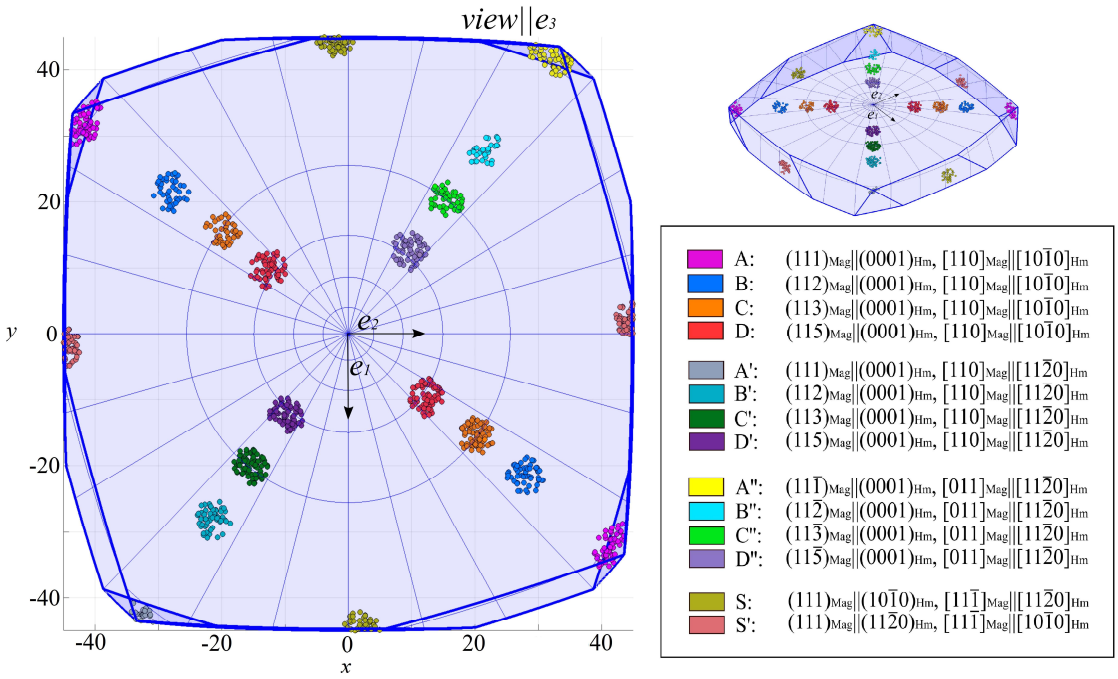

Figure 7: Guide of expected clusters in the misorientation space (cubic-*m*3*m* to trigonal-*3)* for the magnetite-hematite analyses in fundamental zone (Axis-angle). Data is simulated using the orientation relationships from Table 1 and their equivalent ORs in the directions [110] || [11-20], [011] || [11-20] and [01-1] || [10-10].

Table 3: Clustering quantification of the magnetite-hematite grain boundary misorientation analyses.

Grain / OR	Type-A	Type-B	Type-C	Type-D	Type-S	Sum
Grain I	64.66%	0.71%	0.42%	0.26%	9.61%	75.66%
Grain II	38.31%	1.94%	0.77%	3.25%	11.04%	55.32%
Grain III	80.89%	1.92%	0.20%	0.58%	1.39%	84.98%
Grain IV	56.67%	1.75%	0.65%	0.89%	2.70%	62.66%
Grain V	52.85%	2.36%	0.64%	1.09%	2.88%	59.82%
Grain VI	44.85%	4.02%	0.62%	0.68%	2.37%	52.53%
Mean	56.37%	2.11%	0.55%	1.13%	5.00%	65.16%
Matrix 1	3.08%	4.15%	1.14%	1.79%	1.67%	11.83%
Matrix 2	3.61%	7.30%	0.93%	2.46%	2.77%	17.07%
Mean	3.34%	5.72%	1.03%	2.13%	2.22%	14.45%

Among high-index ORs clusters, Type B in the direction $[011]_{Mag} \parallel [11\text{-}20]_{Hem}$ and Type-C have the highest density. Grain 2 from Sample A (***Fig. 8b***) shows, as in the previous grain, strong clustering in the ORs Type-A with high density in the directions $[110]_{Mag} \parallel [11\text{-}20]_{Hem}$ and $[011]_{Mag} \parallel [11\text{-}20]_{Hem}$. Between high-index ORs, Type-B and D clusters are those with the highest density in the three directions $[110]_{Mag} \parallel [10\text{-}10]_{Hem}$, $[110]_{Mag} \parallel [11\text{-}20]_{Hem}$ and $[011]_{Mag} \parallel [11\text{-}20]_{Hem}$.

Differently from the previous grains of Sample A, this grain shows a much lower density of clusters of ORs Type-S. The highest density of points is located in clusters of Type-A in the directions $[110]_{Mag} \parallel [10\text{-}10]_{Hem}$ and $[011]_{Mag} \parallel [11\text{-}20]_{Hem}$, colored in magenta and yellow respectively (Fig. 5b) . High-index ORs are more pronounced in Type-B clusters in the directions $[110]_{Mag} \parallel [11\text{-}20]_{Hem}$ and $[011]_{Mag} \parallel [11\text{-}20]_{Hem}$. Grain IV from Sample-B (Fig. 8d) shows a higher density of clusters of Type-A, in all three directions, and of Type-S. This grain also shows a medium density cluster referred to Type-B, especially in the directions $[110]_{Mag} \parallel [10\text{-}10]_{Hem}$ and $[110]_{Mag} \parallel [11\text{-}20]_{Hem}$, and weak clustering of Type-C and D in the main $[110]_{Mag} \parallel [10\text{-}10]_{Hem}$ direction.

Grain V from Sample B (Fig. 8e), which corresponds to a section of the banding, shows the conventional cluster of Type A and S, with the highest density in the directions $[110]_{Mag} \parallel [11\text{-}20]_{Hem}$ and $[011]_{Mag} \parallel [11\text{-}20]_{Hem}$. Between high-index ORs, Type-B clusters show high density in all three directions, followed by medium to low density Type-C clusters in the directions $[110]_{Mag} \parallel [11\text{-}20]_{Hem}$ and $[011]_{Mag} \parallel [11\text{-}20]_{Hem}$, and Type-D cluster with medium density in the directions $[110]_{Mag} \parallel [10\text{-}10]_{Hem}$, $[110]_{Mag} \parallel [11\text{-}20]_{Hem}$. Between the high-index ORs clusters, only Type B is pronounced, especially in the directions $[110]_{Mag} \parallel [10\text{-}10]_{Hem}$ and $[110]_{Mag} \parallel [11\text{-}20]_{Hem}$.

Overall, the main texture of all analyzed grains is still related to Type-A orientation relationship, responsible for the direct transition between magnetite and hematite. On average they represent 56.36% of total misorientation points plotted into the magnetite-hematite fundamental zone, in a 5^{o} radius of their cluster center. Their texture contribution for the magnetite-hematite grain boundary analysis ranges from 38.31% to 80.89% of total plotted points. Type-S orientation relationships clusters are identified in every sample. These orientations are responsible for 9.61% and 11.04% of total points in a 5^{o} radius from clusters centers. Grains from Sample B show a less pronounced clustering of Type-S, ranging from 1.52% to 2.88% of total plotted points in a 5^{o} radius from clusters centers.

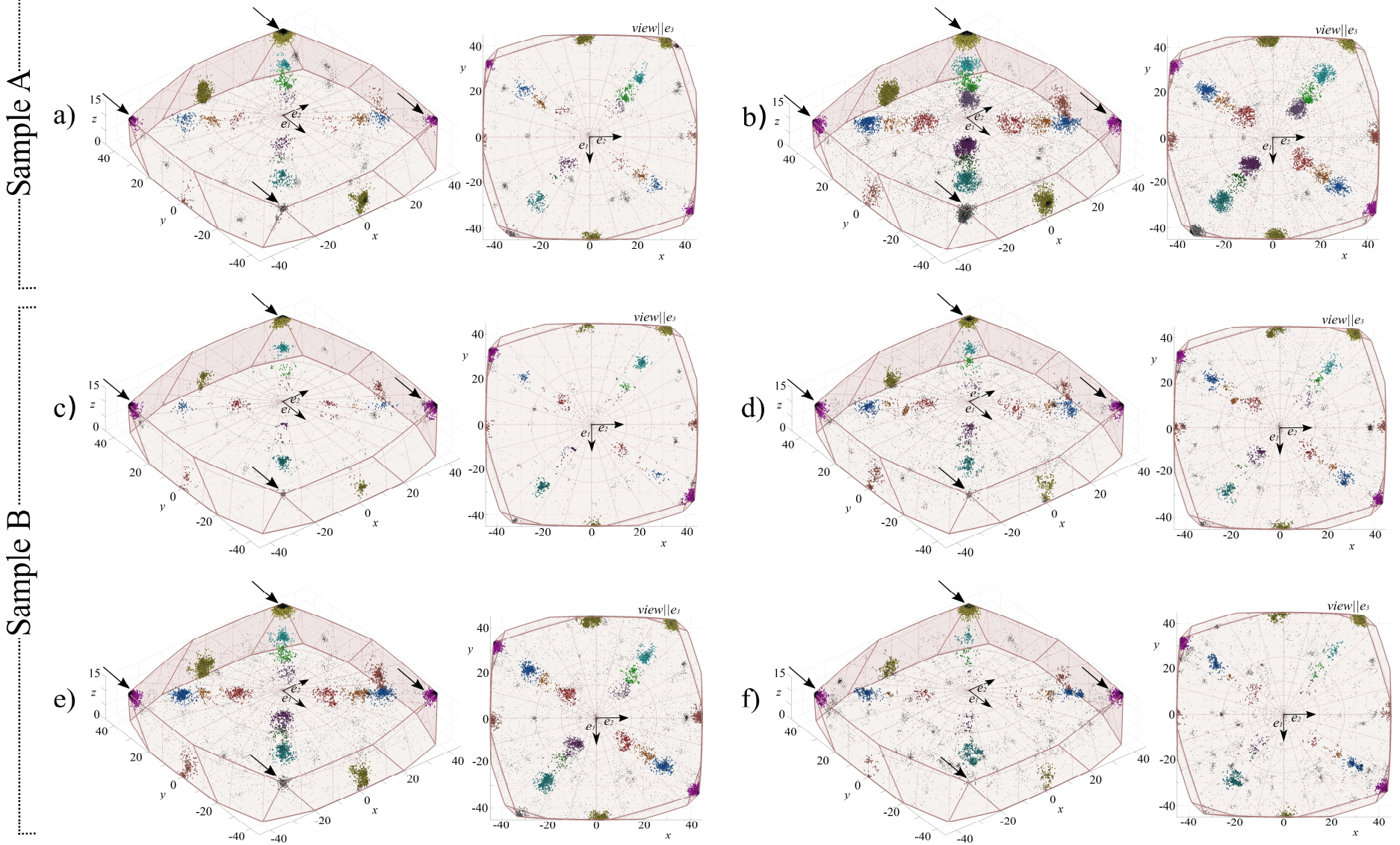

Figure 8: Misorientation distribution of magnetite-hematite boundaries from Sample A and B plotted in the fundamental zone of the axis-angle space. The arrows pointing to clusters are related to the direct phase transformation OR-AA' and their equivalents. Sample A: a) Grain I and b) Grain II. Sample B: c) Grain III, d) Grain IV), e) Grain V and f) Grain VI. The clusters are colored and highlighted by their ORs according to Figure 7.

3.2.2. Hematite-goethite orientation relationships

In **Figure 9a** a visual guide of the expected clusters for the ORs of Table 2 was generated within the appropriate misorientation space for the hematite-goethite crystallographic relationship analysis. The main expected ORs for the hematite-goethite phase transition were called here in this study as OR α and β, for the following crystallographic relationships: $(0001)_{Hem} \parallel (001)_{Ght}$, $[11\text{-}20]_{Hem} \parallel [100]_{Ght}$ and $(0001)_{Hem} \parallel (001)_{Ght}$, $[0\text{-}110]_{Hem} \parallel [100]_{Ght}$ respectively. The OR α and β clusters represent a misorientation with a rotation of 0º and 30º towards *c*-axis respectively. Two pairs of clusters with a rotation of 90º are found in the analyzed data and it is also represented as ORs γ and δ. We called the ORs related to those clusters as Type-γ and Type-δ ORs.

Crystallographic relationships between grain boundaries domains of hematite-goethite inside martitized grains of Sample B were assessed by plotting misorientation data within the corresponding fundamental zone of the Axis-Angle space (**Fig 9b-e**). A table with all orientation relationship of misorientation clusters of grains, misorientation statistics and variations of 5º radius is presented in Table 4.

All analyzed grains present clustering in the orientation relationship α. They are the most evident and dense clusters. The orientation relationship β is also present in most samples, except in Grain IV in which it is absent, although the clustering with a 30º rotation along the *c*-axis is less expressive as the previous OR α. For a better understanding of Type γ-δ ORs, a misorientation analysis of hematite-hematite grain boundaries was also done for possible x-twin identification in the hematite grains that could justify those relationships in the samples (Section 3.2.4).

3.2.3. Magnetite-goethite orientation relationships

Although the direct transition between magnetite and goethite in natural systems has not been described until now, misorientation of grain boundaries between the two extreme points of transformation were analyzed and assessed by plotting them within the appropriate fundamental zone of Axis-Angle space. This was made for a better understanding of the crystallographic relationships between magnetite-hematite-goethite and to check if the crystallographic memory in fact propagates to new phases. Visual guides with simulated clusters were made and can be seen in **Figure 10a.** The chosen

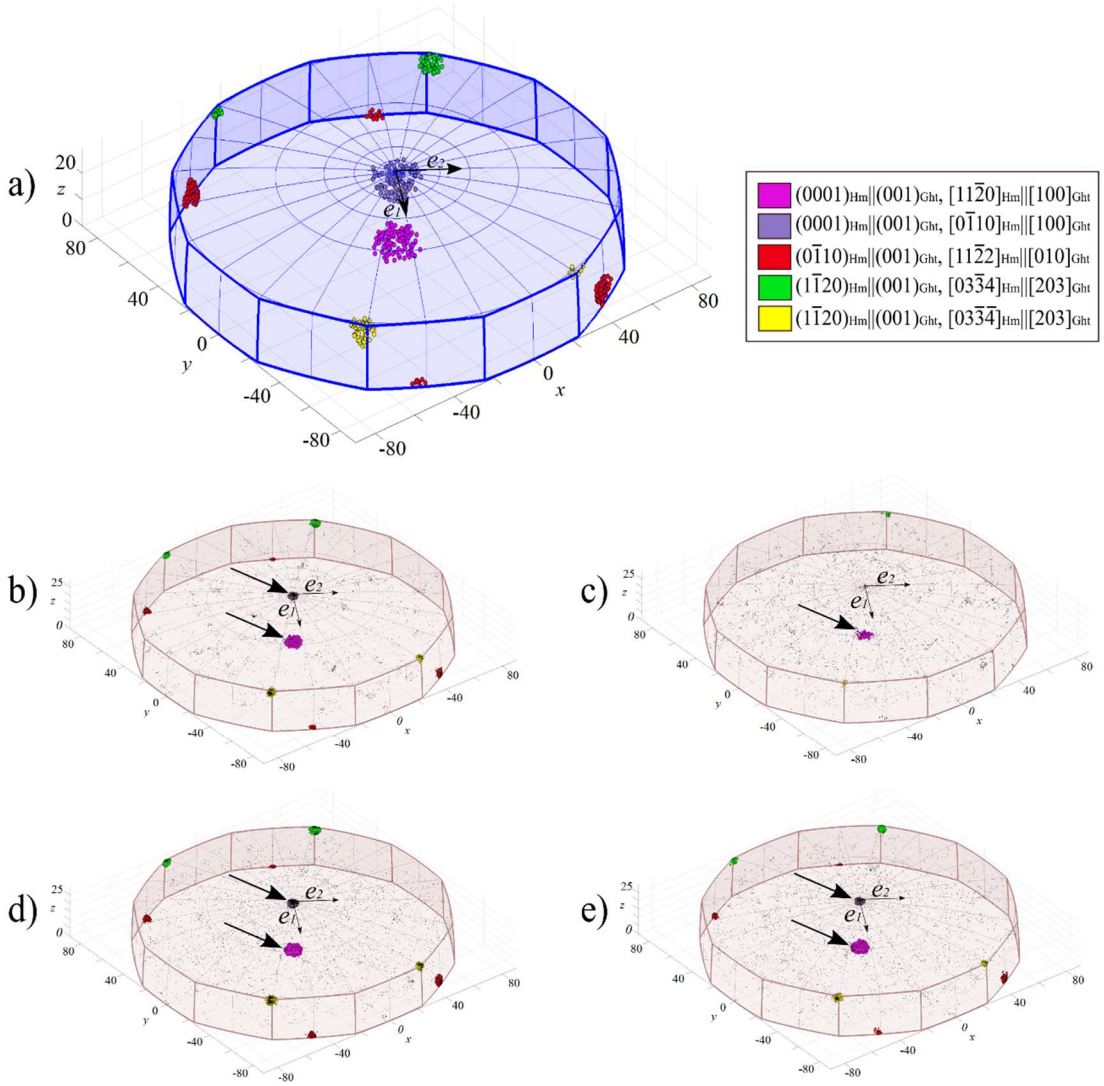

Figure 9: a) Guide of expected clusters in the misorientation space (trigonal-*3* to orthorhombic-222*)* for the hematite-goethite phase transition analysis using the ORs from Table 2 and their equivalent directions; and misorientation distribution of hematite-goethite boundaries from Sample B plotted in the fundamental zone of the axis-angle space, for: b) grain III, c) grain IV, d) grain V and e) grain VI. Arrows pointing to clusters related to the direct phase transformation ORs.

Table 4: Clustering quantification of the hematite-goethite grain boundary misorientation analysis.

Grain / OR	Type-α	Type-β	Type-γ	Sum
Grain III	31.84%	2.91%	15.28%	50.04%
Grain IV	18.17%	1.54%	6.39%	26.11%
Grain V	12.36%	2.08%	9.32%	23.76%
Grain VI	12.49%	2.06%	10.01%	24.56%
Mean	18.71%	2.15%	10.25%	31.11%

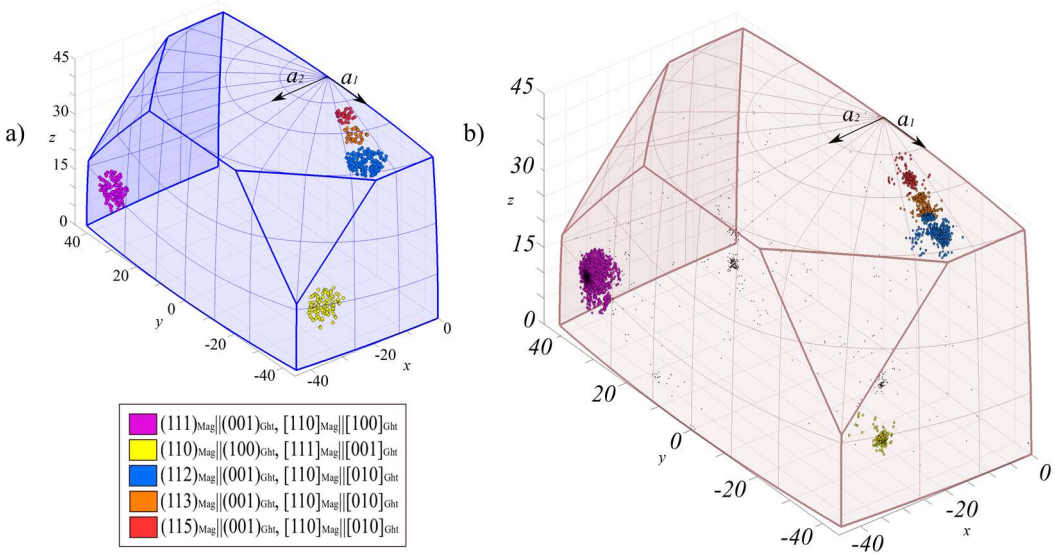

Figure 10: a) Guide of expected clusters in the misorientation space (cubic-*m3m* to orthorhombic-*222*; and b) misorientation distribution of magnetite-goethite boundaries from Grain III - Sample B plotted in the fundamental zone of the Axis-Angle space.

clusters were made by crossing data between those ORs related to topotactic transformation in Table 1 and Table 2. The resulting parallelism of both low- and high-index planes can be seen in the legend of **Figure 10**. and the data were assessed by plotting misorientation of grain boundaries of magnetite-goethite of Grain III in the appropriate fundamental zone (**Fig. 10b)**. Five well-defined clusters can be seen from the given data: the cluster with the highest density among all of them is related to the orientation relationship $(111)_{Mag} \parallel (001)_{Ght}$, $[110]_{Mag} \parallel [100]_{Ght}$, which is a crossing statement between Type A in the magnetite-hematite transition and Type α-β in the hematite-goethite transition, followed by its opposite pair $(110)_{Mag} \parallel (100)_{Ght}$, $[111]_{Mag} \parallel [001]_{Ght}$ colored in yellow in Figure 10. These two clusters share the same rotation angularity of Type A orientation relationship of Table 1 and they sum 7.10% of total plotted points in a 5° radius of the cluster center. High-index orientation relationships can be seen as three clusters in the $[110]_{Mag} \parallel [100]_{Ght}$ direction, related to the orientation relationship of Type B-D and Type α-β. The crystallographic relationship $(112)_{Mag} \parallel (001)_{Ght}$ cluster is the

denser between the high-index planes ORs, although the other two relations can also be seen. The date plotted in **Figure 10b** is in accordance with those found in **Figure 6c**.

3.2.4. Magnetite and hematite twinning

Magnetite-magnetite grain boundaries misorientation of Grain II and V were plotted into the appropriate fundamental zone and compared to the nearest CSL orientation relationship for a better understanding of twinning in both samples (Fig. 11 and Table 5). Misorientations of Grain II from Sample A is divided into five distinct clusters (Fig. 11a), each one of them near a CSL boundary. 58.08% of total misorientation points are located near CSL 3 orientation, situated at a distance of 0.25° from the CSL 3 center and having a radius of 4.96°. This cluster indicates a rotation of 60° along the [111] direction and is correlated to <111>[112] twinning. Near CSL 27b orientation a total of 27.91% of all misorientation points are clustered, 5.59° from CSL 27b center and with a

Table 5: Coordinates in Rodrigues-Frank space and Axis-Angle of cluster center of theoretical CSL boundaries and the nearest clusters to CSL orientation relationships (for magnetite-magnetite analysis) in Grain II and V.

OR	ρ	Axis-Angle
CSL 3	[0.333, 0.333, 0.333]	60,00°
CSL 9	[0.250, 0.250, 0.000]	38,94°
CSL 11	[0.333, 0.333, 0.000]	50,47°
CSL 27b	[0.285, 0.143, 0.000]	35,43°
CSL 29a	[0.400, 0.000, 0.000]	43,60°
CSL 33b	[0.273, 0.091, 0.091]	33,60°
(Grain II)		
n-CSL 3	[0.333, 0.333, 0.333]	60,00°
n-CSL 9	[0.261, 0.257, 0.004]	40,87°
n-CSL 11	[0.359, 0.317, 0.005]	51,21°
n-CSL 27b	[0.262, 0.194, 0.012]	35,21°
n-CSL 33b	[0.264, 0.114, 0.108]	33,88°
(Grain V)		
n-CSL 3	[0.333, 0.333, 0.332]	60,00°
n-CSL 27b	[0.260, 0.194, 0.021]	35,30°
n-CSL 29a	[0.413, 0.000, 0.000]	44,56°

radius of 2.80°. This cluster represents a rotation of 35.1° about the [210] direction and is correlated to <112>[115] twinning. Other three minor clusters can be seen near CSL 9, CSL 11 and CSL 33b. They represent 1.13%, 0.89% and 1.27% of total misorientation points plotted and are located 2.10°, 3.25° and 3.61° from the nearest CSL center, respectively.

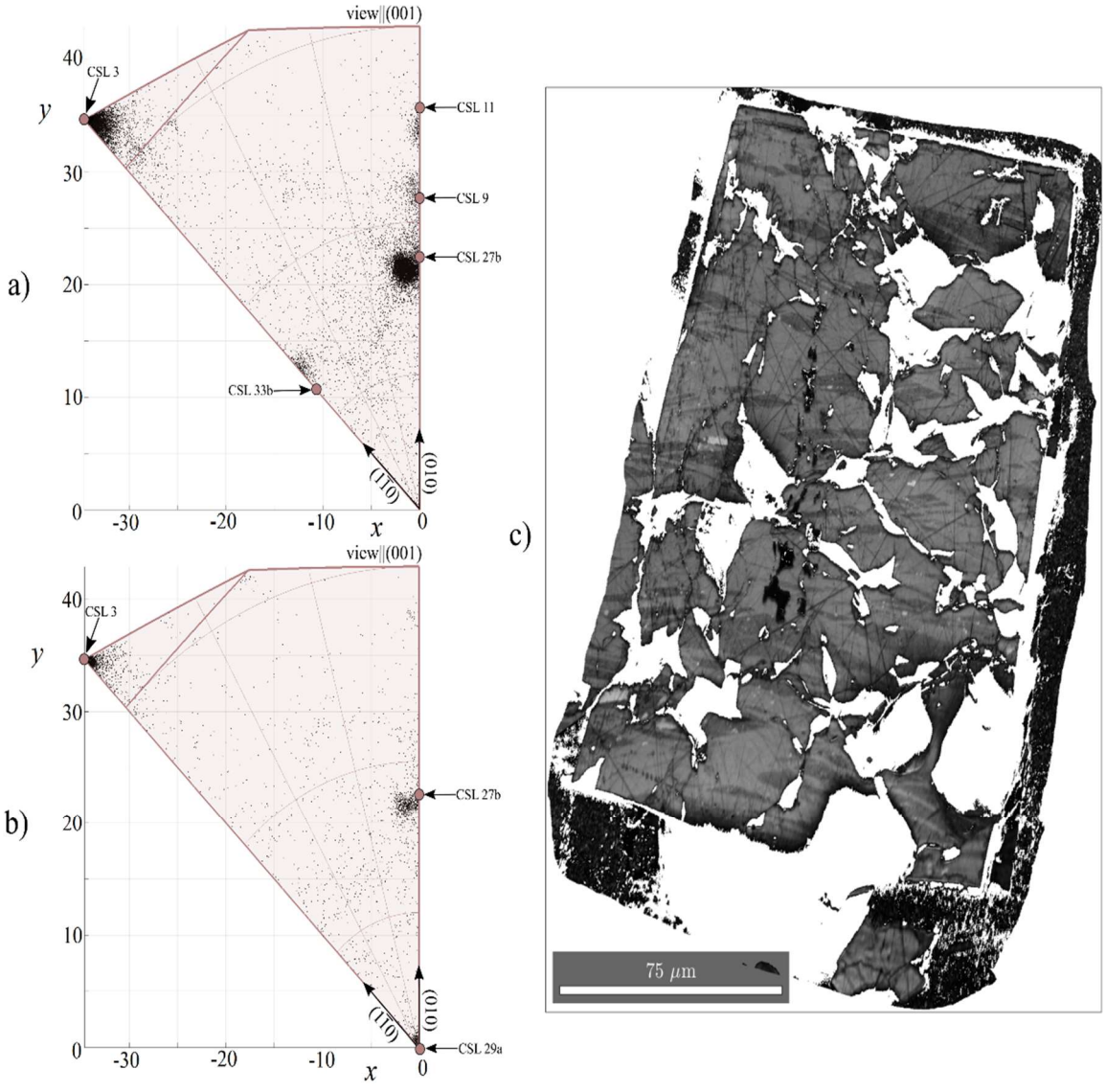

Figure 11: Misorientation distribution of magnetite-magnetite boundaries plotted in axis-angle space with clusters assigned to their CSLs indication (*Table 5*). a) Grain II – Sample A and b) Grain V – Sample B. c) Quality Image Map of Grain II in grayscale showing a lamellar twinning of magnetite.

Misorientations points of Grain V from Sample B (Fig. 11b) indicate three well-defined clusters near the CSL 3, CSL 27b and CSL 29a. Clustering near CSL 3 orientation accounts 44.48% of all plotted points in a 3° radius from cluster center. It has a radius of 3.96° and is located 0.20° from CSL 3 center. The cluster near CSL 27b has 10.44% of all misorientation points and a radius of 1.92°. It is also 5.70° away from CSL 27b center. Differently from the previous sample, Grain V shows a new cluster that coincides with CSL 29a and has 16.46% of all misorientation points. This new cluster has a radius of 1.47° and it is 0.96° away from CSL 29b center.

Hematite-hematite misorientation distribution of Grain V was also analyzed in the appropriate fundamental zone (Fig. 12) and five clusters are identified. Hematite-hematite misorientations present a complex clustering due to the diversity of possibilities of twinning in several directions and forms. Only clusters visually identifiable were chosen. All grains from both samples share the same clusters. The misorientation clusters can be divided into three distinct families. The first family shares the rotation along [0001] direction, responsible for basal twinning (c-twins). Two different rotations can be seen about this axis with 35° and 60° (clusters are colored in pink and yellow respectively, Fig. 12). A second family is identified by a single cluster along the [10-10] direction and a characteristic rotation of 75°; these clusters are related to twinning of prism sections (m-twins) (colored with blue color in Fig. 9). A third family is spotted by two clusters along the directions [11-22] and [12-33] and with a rotation of approximately 90° (green and red colors respectively in Fig. 12).

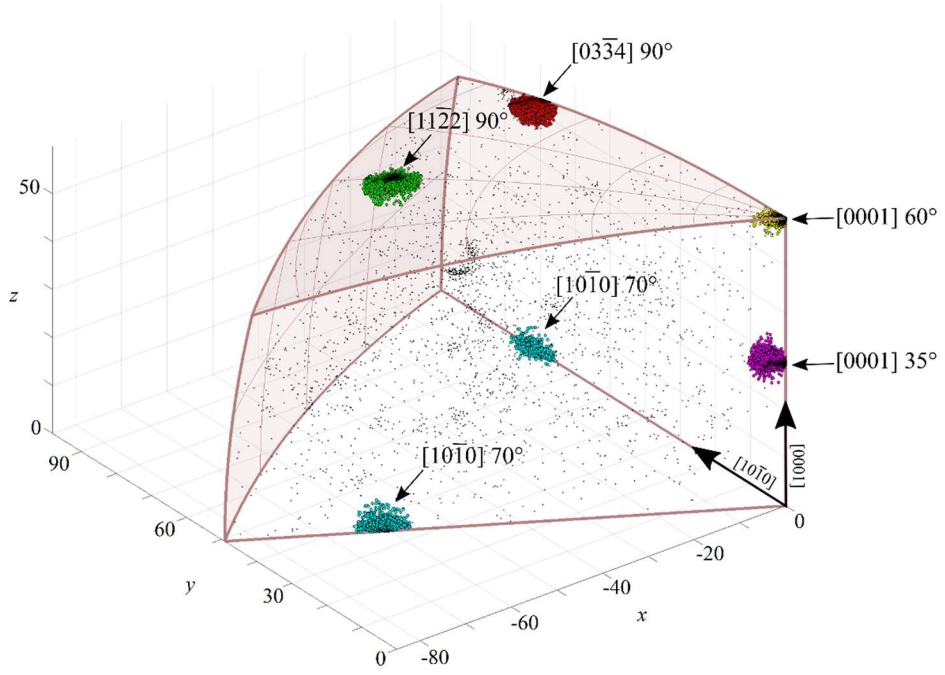

Figure 12: Misorientation distribution of hematite-hematite boundaries of Grain V – Sample B plotted in axis-angle space with clusters assigned to their twinning plane (*Table 4*).

3.2.5. Matrix's magnetite-hematite orientation relationships

As in section 3.2.1, matrix of magnetite-hematite misorientations was also analyzed in the appropriate fundamental zone for comparison purposes with clustering of grains. Differently than the domains of single crystals analyzed before, matrix misorientations show a random distribution of points within the fundamental zone (Fig. 13). The complete data of orientation relationships misorientation clusters of grains, their misorientation statistics and variations in a 5° radius is also presented in Table 3.

The high-index orientation relationships have a prevalent density when compared to Type-A or low-index ORs. Matrix of Sample A (Fig. 13a) has high-index representing 10.68% of the total misorientation points, when compared to only 3.61% of low-index clusters. Within high-index ORs, the highest density of points belongs to Type-B ORs (7.30%) and Type-D (2.46%) (Fig. 11a). Type-C ORs is responsible for 0.93% of total misorientation points. Type-B and D show consistence of density in all directions, with exception of Type-D clusters which have a denser cloud in the $[110]_{Mag} \parallel [10\text{-}10]_{Hem}$ direction. Type-C clusters contributes for only 0.93% of total points, whilst Type-S clusters have 2.77%.

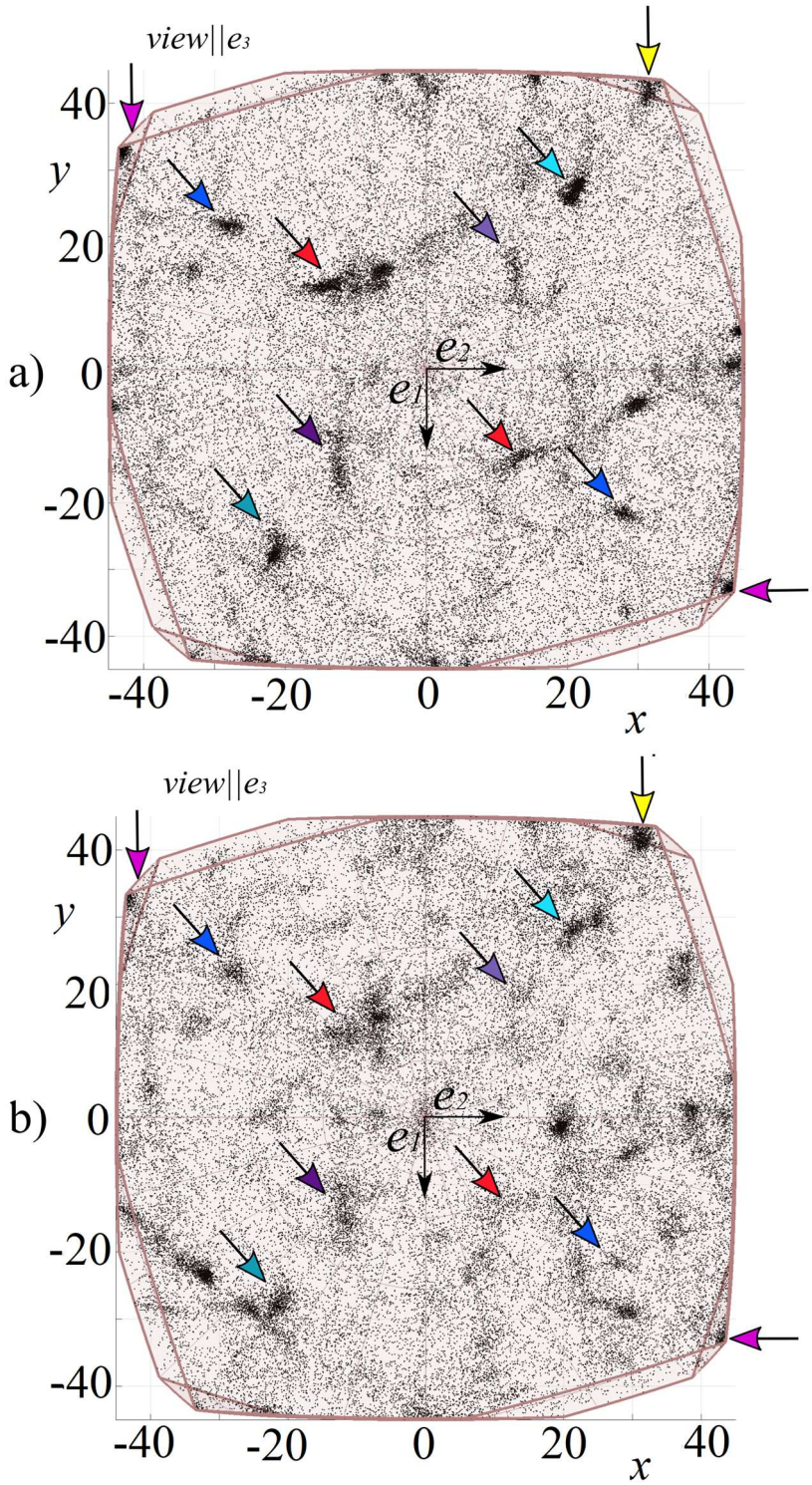

Figure 13: Matrix misorientation distribution of magnetite-hematite boundaries from Sample A (a) and Sample B (b) plotted in the fundamental zone of the axis-angle space. Arrows are colored to the assigned cluster and ORs from Figure 7.

Sample B matrix (Fig. 13b) shows less dense clusters when compared to the previous sample, but high-index orientation relationships still prevails over low-index one (Fig. 11b). Matrix of Sample B has high-index representing 7.08% of the total misorientation points, in opposition to only 3.08% of low-index clusters. Within high-index ORs, the highest density of points belongs to Type-B ORs (4.15%). Type-C and Type-D clusters centers have a total of 1.14% and 1.79% of total plotted points. Within Type-A, the highest density cluster is located along the $[011]_{Mag} \parallel [11\text{-}20]_{Hem}$ direction. Type-B clusters are denser in the $[011]_{Mag} \parallel [11\text{-}20]_{Hem}$ and $[110]_{Mag} \parallel [11\text{-}20]_{Hem}$ directions. Type-S ORs clusters have 1.67% of all plotted points in a 5° radius from their cluster centers. In general, matrix orientation relationships tend to have a greater contribution of Type-B relationships than topotactically ORs of Type-A, being Type-B 1.3 to 2 times higher in proportion of points. Both OR are the most important crystallographic texture in the matrix's magnetite-hematite misorientation analysis. Sample A shows a higher density of Type-D and Type-S clusters when compared to Sample B, but they still share consistency with high-index OR overcoming Type-A in total points plotted, specially Type-B orientation relationships.

3.3. Mineral Characterization of the N4WS Drill core

Major element geochemistry of 156 samples were analyzed and, in Table 6, the data from 14 samples were selected, differently from the previous two samples used for EBSD analysis. The average results of every 20 meters' intervals are also shown in Table 7. Ore canga rocks show averagely SiO_2 content of 0.52%, 3.76% of Al_2O_3, 87.71% of Fe_2O_3 and 0.72% of P_2O_5 ≈. The rocks from the shallowest level of the studied drill core present the highest values for Al_2O_3, P_2O_5. It is an iron-rich ore, oxide facies, but registering a concentration of aluminum and phosphorus. The underlying sequence, the friable hematite ore shows also low SiO_2 content, ranging from 0.06% to 0.95%. It has significantly low content of Al_2O_3 and P_2O_5 when compared to the superimposed ore canga: 0.12-0.26% and 0.01-0.08% respectively. At this interval, concentration of Fe_2O_3 reaches its maximum values between 95.78% and 97.93% of bulk composition. Jaspilite rocks show high content of silica (36.70% to 46.90%) and iron oxide (51.36 to 59.18%). SiO_2 and Fe_2O_3 contents comprise most of its bulk composition. The classification of these select samples are based on their oxides content obtained with ICP-AES data and shows a good correlation with the same classification obtained by Prado et al. (2016) with reflectance spectroradiometry data.

Table 6 - Major elements geochemistry of selected samples of the N4WS F1051 drill core

Sample	Depth	Rock	SiO_2	TiO_2	Al_2O_3	Fe_2O_3	MnO	MgO	CaO	Na_2O	K_2O	P_2O_5	LOI	Total
F1051-004	06 - 08	**OC**	0.42	0.39	2.21	90.32	0.03	0.01	0.01	0.00	0.01	0.762	4.77	98.93
F1051-008	14 - 16	**OC**	052	0.47	1.89	89.84	0.03	0.02	0.01	0.00	0.01	0.632	4.68	99.73
F1051-020	38 - 40	**HF**	0.72	0.02	0.14	97.20	0.02	0.02	0.01	0.00	0.01	0.046	1.54	99.73
F1051-034	66 - 68	**HF**	0.69	0.01	0.09	97.22	0.02	0.03	0.01	0.01	0.01	0.037	2.80	100.93
F1051-049	96 - 98	**HF**	0.79	0.00	0.16	97.06	0.03	0.03	0.01	0.01	0.01	0.04	2.73	100.87
F1051- 064	126 - 128	**HF**	0.75	0.00	0.08	96.07	0.27	0.02	0.01	0.01	0.01	0.019	2.94	100.18
F1051-078	154 - 156	**HF**	0.54	0.00	0.11	97.65	0.06	0.03	0.01	0.01	0.00	0.013	2.01	100.43
F1051-094	186 - 188	**HF**	1.93	0.01	0.13	97.70	0.06	0.03	0.01	0.00	0.01	0.009	1.12	101.01
F1051-101	200 - 202	**JP**	40.81	0.00	0.00	57.96	0.02	0.05	0.01	0.00	0.00	0.008	1.78	100.64
F1051-110	218 - 220	**JP**	42.34	0.00	0.01	56.83	0.02	0.04	0.01	0.00	0.00	0.005	0.97	100.23
F1051-115	228 - 230	**JP**	36.03	0.00	0.07	62.40	0.03	0.06	0.01	0.00	0.00	0.08	1.44	100.12
F1051-124	246 - 248	**JP**	39.79	0.00	0.14	59.41	0.02	0.05	0.03	0.00	0.00	0.007	0.89	100.34
F1051-139	276 - 278	**JP**	45.56	0.00	0.02	51.85	0.09	1.82	0.08	0.00	0.01	0.036	1.00	100.47
F1051-151	300 - 302	**JP**	46.49	0.00	0.02	48.79	0.16	0.69	1.27	0.00	0.00	0.012	2.74	100.17

Table 7 - Average major elements geochemistry of every 20m interval of the N4WS F1051 drill core.

Depth (m)	Rock	SiO_2	TiO_2	Al_2O_3	Fe_2O_3	MnO	MgO	CaO	Na_2O	K_2O	P_2O_5	LOI	Total
01- 20	**OC**	0.52	0.59	3.76	87.71	0.04	0.02	0.01	0.00	0.01	0.724	6.468	99.84
20 - 40	**HF**	0.82	0.03	0.26	96.74	0.03	0.02	0.01	0.00	0.02	0.071	2.14	100.13
40 - 60	**HF**	0.84	0.02	0.25	97.17	0.34	0.04	0.01	0.02	0.01	0.076	1.457	100.23
60 - 80	**HF**	0.95	0.01	0.21	96.46	0.11	0.04	0.02	0.02	0.01	0.053	2.577	100.47
80 - 100	**HF**	0.78	0.00	0.12	96.46	0..03	0.04	0.01	0.01	0.01	0.039	2.983	100.48
100 - 120	**HF**	0.77	0.00	0.17	96.36	0.04	0.02	0.01	0.00	0.00	0.036	2.778	100.19
120 - 140	**HF**	0.78	0.00	0.25	95.78	0.39	0.03	0.01	0.01	0.01	0.031	3.052	100.34
140 - 160	**HF**	0.60	0.00	0.15	97.77	0.16	0.03	0.01	0.01	0.00	0.018	1.576	100.33
160 - 180	**HF**	0.71	0.00	015	97.93	0.30	0.03	0.01	0.02	0.00	0.009	1.201	100.35
180 - 200	**HF/JP**	11.96	0.00	0.24	86.56	0.13	0.04	0.01	0.00	0.01	0.011	1.279	100.25
200 - 220	**HF/JP**	19.67	0.01	0.19	78.78	0.12	0.06	0.06	0.01	0.01	0.019	1.428	100.33
220 - 240	**JP**	38.72	0.00	0.01	59.18	0.03	0.05	0.01	0.00	0.00	0.009	2.107	100.11
240 - 260	**JP**	44.21	0.05	1.60	52.50	0.04	0.55	0.02	0.01	0.25	0.021	1.128	100.37
260 - 280	**JP**	46.90	0.00	0.03	51.36	0.07	0.70	0.10	0.00	0.01	0.023	1.178	100.35
280 - 300	**JP**	42.74	0.00	0.01	52.04	0.19	2.06	1.30	0.00	0.01	0.015	1.796	100.16
300 - 320*	**JP**	36.70	0.03	0.03	54.49	0.30	2.50	2.58	0.01	0.00	0.010	3.56	100.21

* only banded iron formations were selected in this interval

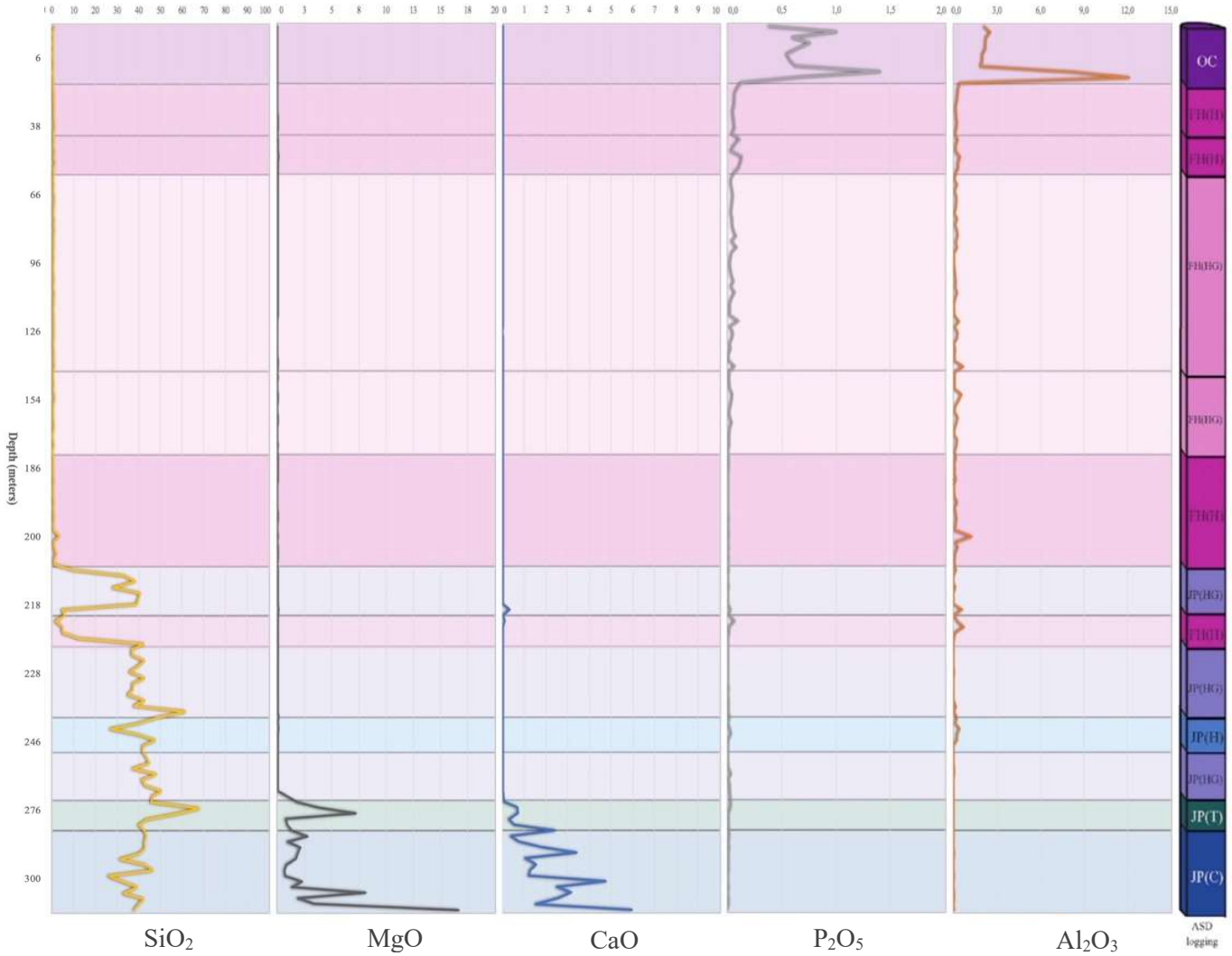

Figure 14: Vertical geochemistry analyses of SiO_2, MgO, CaO, P_2O_5, Al_2O_3 and ASD logging (adapted from Prado et al. 2016) from the drill core F1051 (N4WS), Serra Norte deposit.

Representative Mössbauer spectra of the samples F1051-004, F1051-078 and F1051-151 from Ore Canga (OC), Friable Hematite (HF) and Jaspilite (JP) are shown in Figure 15. The hyperfine parameters of all samples obtained are shown in Table 8. The best fits (Fig. 15a) for Ore Canga sample (F1051-004) are: one sextet corresponding to parameters IS= 0.37, QS=-0.19 and BHF=51.0; a duplet of parameters IS= 0.25 and QS=-0.57. The sextet corresponds to hematite (α-Fe2O3) (Tucek et al. 2013) and the duplet, to goethite (α-FeOOH) (Nayak et al. 2011, Murad & Schwertmann 1983). The relative concentrations of hematite and goethite are 84.5% and 15.5% respectively. The goethite is represented by duplet and not by a normal sextet. This is attributed to its microcristallinity and Al-substitution (Nayak et al. 2011, Murad & Schwertmann 1983).

The Friable Hematite samples always show two or one sextets with the following mean parameters (Fig. 3b): IS= 0.38, QS=-0.28, BHF=38.1 and IS= 0.37, QS=-0.19, BHF=51.3. Those sextets correspond to goethite (α-FeOOH) and hematite (α-Fe2O3) respectively (Tucek et al. 2013). By its relative mineral concentration, the Friable Hematite can be divided into two main types based on the concentration of hematite: in the first one, the concentration of goethite is less than 20% and of hematite is higher than 80%, reaching 100% of hematite at 186 m (sample F1051-094), and in the second type, the concentration of goethite reaches around 25% and, of hematite, approximately 75% (Fig. 16). These two types correspond, as described in Prado et al. (2016).

The remaining samples are assigned as the protore or Jaspilite (JP) (Table 8) and three main Mössbauer spectra were obtained. The best fit spectra of samples F1051-101 and F1051-110 are referred to the two sextets and their mean hyperfine parameters IS= 0.37, QS=-0.20, BHF=51.4 and IS= 0.36, QS=-0.27, BHF=37.8 and they correspond to hematite (α-Fe2O3) and goethite (α-FeOOH) respectively (Tucek et al. 2013). Their content of hematite and goethite correspond averagely to 81.75% and 18.25%, respectively. These samples were classified, after Prado et al. (2016) as JP (HG), a jaspilite containing both hematite and goethite. The spectra of samples F1051-115, F1051-124 and F1051-139 present only one sextet defined by the mean hyperfine parameters IS= 0.37, QS=-0.18 and BHF=51.3, attributed to hematite (α-Fe2O3) (Tucek et al. 2013). This means that other mineral phases as goethite and magnetite are non-present or below the technique detection limit (4%). These rocks are referred by Prado et al. (2016) as JP (H), a jaspilite containing mostly hematite.

Table 8 - Mössbauer Spectrometry Parameters for the N4WS – F1051

Sample	Depth (meters)	Rock	Temp. (K)	IS (mm/s)	QS (mm/s)	LWD (mm/s)	BHF (T)	Area (%)	Phase
F1051-004	06 - 08	OC	300	0.37	-0.19	0.42	51	84.5	Hematite
				0.25	-0.57	0.,41	-	15.5	Goethite*
F1051-020	38 - 40	HF	300	038	-0.31	0.70	38.1	13.6	Goethite
				036	-0.19	0.37	51.3	86.4	Hematite
F1051-034	66 - 68	HF	300	0.36	-0.28	0.43	37.9	25	Goethite
				0.37	-0.19	0.36	51.4	75	Hematite
F1051-049	96 - 98	HF	300	0.38	-0.27	0.52	37.9	24	Goethite
				0.37	-0.19	0.34	51.3	76	Hematite
F1051- 064	126 - 128	HF	300	0.37	-0.27	0.44	37.9	25.1	Goethite
				0.37	-0.19	0.32	51.3	74	Hematite
F1051-078	154 - 156	HF	300	0.37	-0.27	0.46	37.7	20.3	Goethite
				0.37	-0.19	0.34	51.2	79.7	Hematite
F1051-094	186 - 188	HF	300	0.36	-0.19	0.37	51.3	100	Hematite
F1051-101	200 - 202	JP	300	0.37	-0.35	0.46	37.7	17	Goethite
				0.37	-0.2	0.34	51.4	83	Hematite
F1051-110	218 - 220	JP	300	0.36	-0.27	049	37.8	19.5	Goethite
				0.37	-0.2	0.32	51.4	80.5	Hematite
F1051-115	228 - 230	JP	300	0.36	-0.19	0.36	51.3	100	Hematite
F1051-124	246 - 248	JP	300	0.37	-0.18	0.37	51.3	100	Hematite
F1051-139	276 - 278	JP	300	0.37	-0.18	0.35	51.4	100	Hematite
F1051-151	300 - 302	JP	300	0.66	-0.01	0.41	45.5	40.9	Fe^{3+} in A-sites of magnetite
				028	0.002	0.36	48.8	27	$Fe^{3+} + Fe^{2+}$ in B-sites of Magnetite
				036	-0.19	0.29	51.2	32.1	Hematite

* Microcrystalline goethite and/or Al substituted

The jaspilite in its most typical mineral assemblage is evidenced only at depths bellow 300 m using Mössbauer Spectrometry. The best fit of sample F1051-151 correspond to three sextets (Table 8; Fig. 15c): two from magnetite representing Fe^{3+} in A-sites (hyperfine parameters IS= 0.28, QS=0.002, BHF=48.8) and $Fe^{3++}Fe^{2+}$ in B-sites (parameters IS= 0.66, QS=-0.01, BHF=45.5); and one from hematite (hyperfine parameters IS= 0.36, QS=-0.19, BHF=51.2) (Tucek et al. 2013). The relative concentration of magnetite is given by the sum of the area of the two sextets which correspond to 67.9% in this sample. On the other hand, hematite has a relative concentration of 32.1%. Maghemite phase was not seen in any spectrum, including the jaspilite.

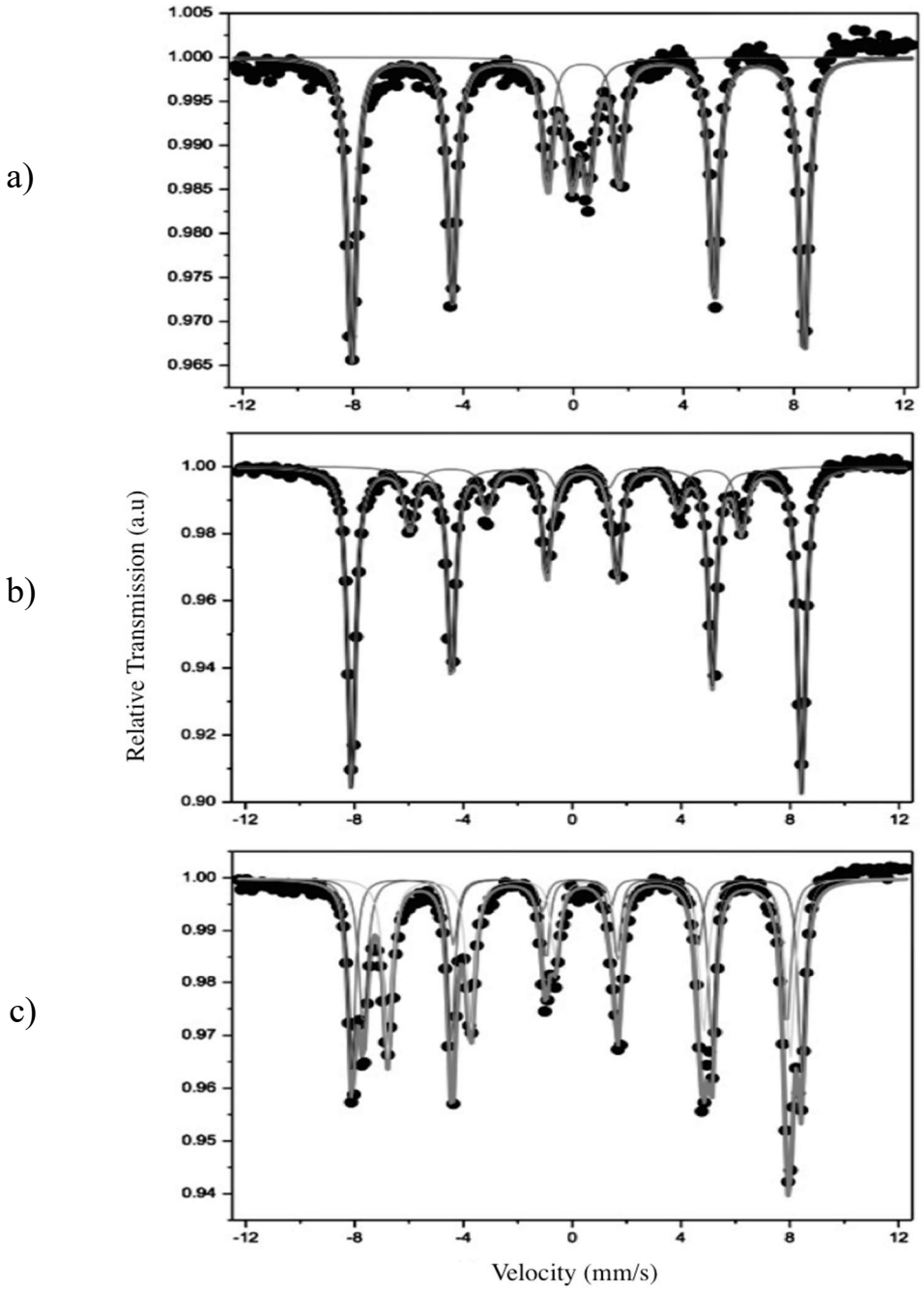

Figure 15: Most representative room temperature Mössbauer spectra of the main three lithotypes of the iron ore: A) Ore Canga (OG); *sample F1051-004* B) Friable Hematite; *sample F1051-078* (FH) and C) Jaspilite (JP); *sample F1051-151*

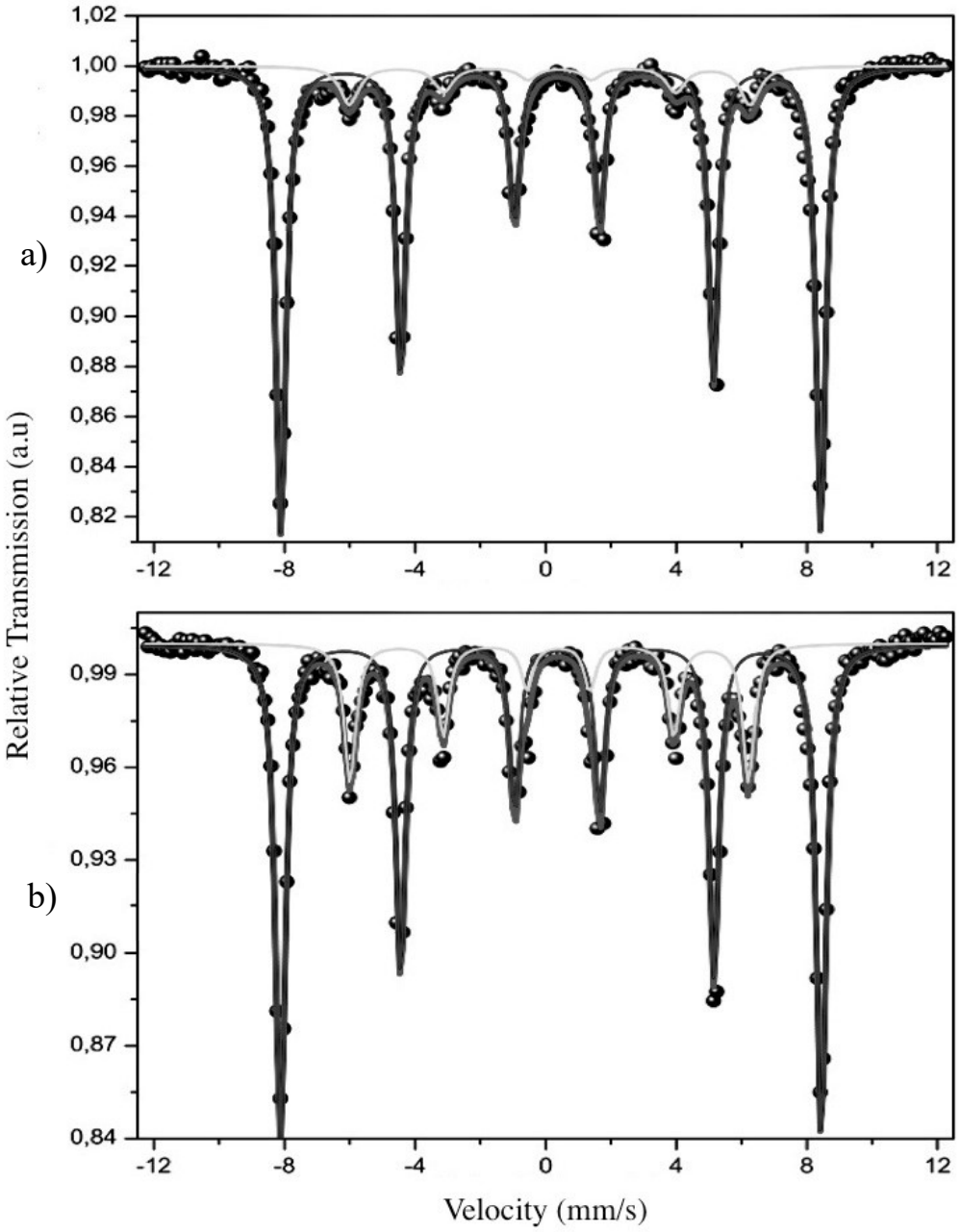

Figure 16: Mössbauer spectra showing the differences between Friable Hematite ores: A) Friable Hematite ore with high hematite and low goethite concentration; sample F1051-020; B) Friable Hematite ore with high hematite and intermediate goethite concentration; sample F1051-034.

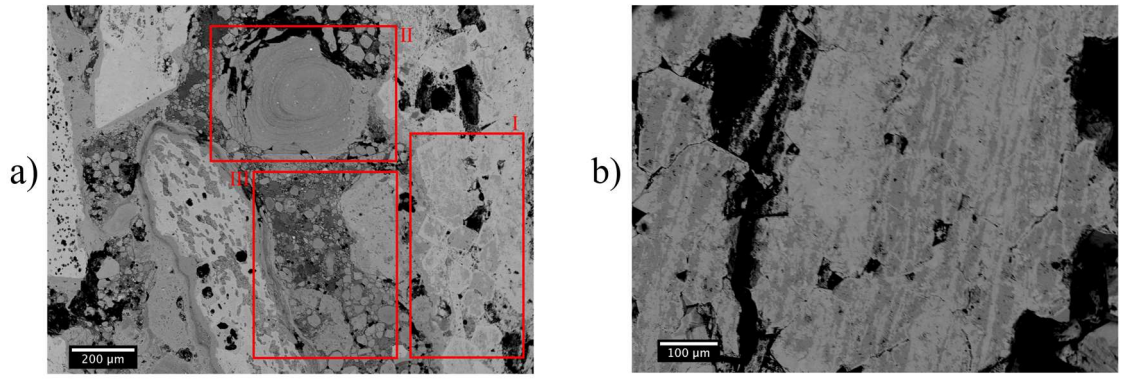

Figure 17: a) Back-scattered electron image of ore canga sample F1051-12 showing the analyzed domains in the electron microprobe analysis: I – preserved martite crystals with the typical phase transformation texture between hematite and goethite, II – Concentric goethite aggregate, III – goethite aggregate. b) Backscatter image of friable hematite sample F1051-46 showing its most common texture of elongated crystals of hematite and transformed goethite.

Four samples were selected for EPMA analysis of hematite and goethite (Table 9). It was called transformed hematite and goethite, the minerals with an evident phase transformation relationship as represented before in Figures 4 and 5. Goethite forming aggregates and concentric structures were also analyzed. BSE images (Fig. 17a) of Domain I evidence goethite inside hematite grains in a texture of phase transformation; and of Domains II and III show goethite particles in a polycrystalline aggregate. Martitized grains with hematite and goethite from friable hematite ore can be seen in Figure 17b.

The samples were chosen by their texture and mineral association. All goethite grains from the jaspilite (Sample F1051-101) are associated with hematite grains and show low content of P_2O_5 and Al_2O_3. The goethite from the hematite ore shows similar composition, specially the absence of P_2O_5 and Al_2O_3. The textures seen in the friable ore (Fig. 17b) are also very similar to those found in the jaspilites described here before in section 3.1.2. In both jaspilite and hematite, goethite shows similar composition of P_2O_5 and Al_2O_3 as the surrounding hematite. During ore canga analysis, both textures can be seen in the Samples F1051-4 and F1051-12: still preserved martitized grains with evident transformation relationship and goethite aggregates. The aggregates of goethite have a significant increase in P_2O_5 and Al_2O_3 while goethite and hematite of transformation domains has similar composition as the oxides/hydroxides of the jaspilite and friable hematite ore

Table 9 – Electron microprobe analysis of hematite and goethite by different textures and lithotypes.

Mineral Texture Type	Transf. Hematite	Transf. Hematite	Transf. Hematite	Transf. Hematite	Transf. Hematite	Transf. Hematite	Transf. Goethite	Transf. Goethite	Transf. Goethite	Transf. Hematite
Sample	F1051-101	F1051-101	F1051-101	F1051-101	F1051-101	F1051-101	F1051-101	F1051-101	F1051-101	F1051-46
Depth (meters)	200 - 202	200 -202	200 -202	200 -202	200 -202	200 -202	200 -202	200 -202	200 -202	96 - 98
Rock	Jaspilite	Jaspilite	Jaspilite	Jaspilite	Jaspilite	Jaspilite	Jaspilite	Jaspilite	Jaspilite	Friable Hem.
MgO	0.21	0.00	0.01	0.00	0.03	0.01	0.00	0.00	0.00	0.04
Al_2O_3	0.00	0.00	0.00	0.02	0.00	0.02	0.00	0.00	0.00	0.04
SiO_2	1.15	0.17	3.36	1.10	0.15	0.41	0.73	1.00	0.84	110
P_2O_5	0.00	0.02	0.00	0.00	0.02	0.00	0.01	0.00	0.00	0.00
TiO_2	0.20	0.02	0.01	0.06	0.21	0.06	0.00	0.00	0.09	0.01
FeOT	89.10	88.87	86.75	87.13	88.73	89.59	77.42	77.95	77.33	84.61
Total	90.81	89.26	90.21	88.48	89.35	90.23	78.23	79.01	78.40	85.94

Mineral Texture Type	Transf. Hematite	Transf. Goethite	Transf. Goethite	Transf. Goethite	Transf. Goethite	Transf. Goethite	Transf. Hematite	Transf. Hematite	Transf. Goethite	Transf. Goethite
Sample	F1051-46	F1051-46	F1051-46	F1051-46	F1051-46	F1051-46	F1051-12	F1051-12	F1051-12	F1051-12
Depth (meters)	96 - 98	96 - 98	96 - 98	96 - 98	96 - 98	96 - 98	14 - 16	14 - 16	14 - 16	14 - 16
Rock	Friable Hem.	Friable Hem.	Friable Hem.	Friable Hem.	Friable Hem.	Friable Hem.	Ore Canga	Ore Canga	Ore Canga	Ore Canga
MgO	0.00	0.00	0.02	0.00	0.05	0.01	0.06	0.00	0.07	0.04
Al_2O_3	0.05	0.01	0.07	0.09	0.02	0.07	0.14	0.15	0.11	0.28
SiO_2	1.33	1.21	1.11	1.04	1.06	0.89	0.94	0.90	0.72	0.94
P_2O_5	0.00	0.00	0.00	0.03	0.04	0.00	0.17	0.21	0.02	0.13
TiO_2	0.17	0.00	0.26	0.27	0.26	0.00	0.12	0.13	0.09	0.13
FeOT	83.51	76.81	73.88	74.08	74.99	74.09	88.03	88.35	78.24	79.18
Total	85.37	78.37	75.58	75.58	76.98	75.23	89.50	89.93	79.57	80.94

Mineral Texture Type	Goethite Aggregate	Goethite Aggregate	Goethite Aggregate	Goethite Aggregate	Goethite Aggregate	Goethite Aggregate	Goethite Aggregate	Goethite Aggregate	Transf. Hematite
Sample	F1051-12	F1051-12	F1051-12	F1051-12	F1051-12	F1051-12	F1051-12	F1051-12	F1051-04
Depth (meters)	14 - 16	14 - 16	14 - 16	14 - 16	14 - 16	14 - 16	14 - 16	14 - 16	06/ago
Rock	Ore Canga	Ore Canga	Ore Canga	Ore Canga	Ore Canga	Ore Canga	Ore Canga	Ore Canga	Ore Canga
MgO	0.03	0.02	0.01	0.00	0.05	0.03	0.00	0.02	0.04
Al_2O_3	3.02	3.66	3.87	4.84	2.95	3.48	3.68	3.44	0.06
SiO_2	0.09	0.10	0.08	0..07	0.09	0.05	0.03	0.12	0.22
P_2O_5	1.88	1.58	2.20	1.87	1.71	2.23	1.91	1.92	0.00
TiO_2	0.89	0.77	0.34	0.27	0.45	0.57	0.39	0.95	0.25
FeOT	73.27	75.19	74.96	71.73	78.22	74.83	76.05	72.24	87.87
Total	79.58	81.70	81.76	78.99	83.74	81.79	82.17	79.03	88.79

Mineral Texture Type	Transf. Hematite	Transf. Hematite	Transf. Goethite	Transf. Goethite	Goethite Aggregate	Goethite Aggregate	Goethite Aggregate	Goethite Aggregate	Goethite Aggregate
Sample	F1051-04	F1051-04	F1051-04	F1051-04	F1051-04	F1051-04	F1051-04	F1051-04	F1051-04
Depth (meters)	06 - 08	06 - 08	06 - 08	06 - 08	06 - 08	06 - 08	06 - 08	06 - 08	06 - 08
Rock	Ore Canga	Ore Canga	Ore Canga	Ore Canga	Ore Canga	Ore Canga	Ore Canga	Ore Canga	Ore Canga
MgO	0.17	0.03	0.00	0.05	0.03	0.08	0.08	0.05	6
Al_2O_3	0.06	0.01	0.16	0.26	2.33	146	1.53	1.46	3.58
SiO_2	0.39	1.01	0.23	0.84	0.12	0.30	0.32	0.33	0.12
P_2O_5	0.02	0.00	0.21	0.04	1.43	0.65	0.75	0.55	1.77
TiO_2	0.00	0.16	0.08	0.17	2.66	2.00	2.29	2.33	1.40
FeOT	89.14	88.73	81.96	79.90	72.02	83.12	83.25	83.11	70.14
Total	89.90	90.07	83.02	81.46	79.10	88.22	88.57	88.14	77.40

4. Discussion

4.1. Crystallographic Textures and Orientation Relationships

Orientation relationships between low-index planes can be easily recognized in pole plot figures of all grains analyzed from both samples by coincidental maxima. This preliminary analysis is already satisfactory to evidence an orientation between the planes $(111)_{Mag} \parallel (0001)_{Hem} \parallel (001)_{Ght}$; $[110]_{Mag} \parallel [10\text{-}10]_{Hem} \parallel [010]_{Ght}$ which can be linked with the pairs of topotactic transformation of magnetite-hematite and hematite-goethite (described in Davis 1968, Cudennec & Lecerf 2005, Barbosa & Lagoeiro 2009), process commonly named as martitization. Those orientation relationships can also be recognized and quantified in misorientation analysis within their appropriate fundamental zone and in pairs. This is an evidence that in the martitized grains where the three phases coexist the basal planes of goethite coincides with basal planes of hematite, and the basal planes of hematite coincides with octahedral planes of magnetite. No evidence of intermediate and metastable phase of maghemite is found in this study.

The first orientation relationship responsible for the martitization process is the OR $(111)_{Mag} \parallel (0001)_{Hem}$, $[110]_{Mag} \parallel [10\text{-}10]_{Hem}$, here assigned as Type-A clusters. This is the only OR that shows the expected topotaxic relationships according to Bursill & Withers (1979). Type-A OR is the most common texture in all analyzed grains, contributing from 38.31% to 80.89% to the total misorientation plotted points of the magnetite-hematite interface. The transition between these two minerals and their crystallographic memories are responsible for the main crystallographic texture of the iron formations of the N4WS deposit. Type-A OR is the most common texture among grains due to its abundance. This OR indicates topotaxity between grains of magnetite and hematite in the deposit, which are mainly located inside martitized grains.

The multiple orientation relationships of high-order contribute in a minor way for the bulk texture of grains, ranging from 1.38% to 5.95% of total plotted points, although they are still distinguishable from random oriented misorientation points. Type-B orientations are more pronounced in grains belonging to banding domains, especially Grain V and VI which have a total percentage of 2.36% and 4.02% of total points related to clusters of high-order in B. Type-C clusters are not very well-developed in any samples, always ranging from 0.20% to 0.77% of total plotted points. Type-D cluster is

more frequent than the previous ORs. The total percentage of Type-D cluster ranges from 0.26% to 3.25% of total plotted points and have an average value of 1.13%. The highest value for Type-D clustering belongs to Grain II from Sample A. For a better understanding of the high-order orientation relationships a further analysis of magnetite-magnetite and hematite-hematite grain boundaries is required for identification of twining near CSL boundaries in magnetite and recrystallization twins in hematite. These high-order ORs which are less expressive than Type-A do not indicate topotaxity in the samples, but evidence the complex rebalance twinning system of magnetite and hematite crystals when exposed to different temperatures of reduction conditions in a successive phase transformation cycle (Modaressi *et al.* 1989 and Whiters & Bursil 1979).

Due to the large overlap of orientation relationships and transformation cycles, it is not possible to verify a genetic relationship between the phases, only that the remnants of such ORs are still preserved in grains of the N4WS deposit. The Serra Norte iron formations are known for their highly preserved jaspilites and for the low intensity of regional metamorphism, unlike iron formations of the QF in which metamorphism was responsible for intensifying the magnetite-hematite transformation (Lagoeiro, 1998).

Whiters & Bursill (1979) used a matrix transformation technique for a better understanding of high order orientation relationships such Type-B to D and the possible models for orientation relationships between magnetite and hematite. Our analyses of natural samples are in consonance with experimental data modeled by their studies, in which transformation-induced orientation relationships were best fitted in a quaternary orientationship Hem/Mag_A/Mag_T/Hem'/Mag_B. This most plausible quaternary orientationship can be represented as misorientation clusters by the presence of Type-A, Type-B, Type-D and Type-S clusters and explained as follows: topotactic transformation of hematite into magnetite followed by twinning of magnetite (Hem/Mag_A/Mag_T) on (-111), represented by Type-A and D clusters, and finally recrystallization of hematite followed by a recrystallization of magnetite forming Type-B and consequentially Type-S clusters (Hem'/Mag_B) (Fig. 18). Whiters & Bursill (1979) confirm in their study that Type-D OR is a more reasonable orientation than Type-C, representing a consequence of the first one. Type-B, D and S high-order orientation are an indicative of a complex process of transformation twinning in between the process of topotactic transformation of magnetite and hematite. Type-B orientations are frequently observed in higher temperatures of reduction (773-1273K) and Type-C and D orientations, in moderate

temperatures (473-673K), where CO/CO_2 gas works as buffers for reduction (Bursill & Whiters, 1979).

Grains I and II show a higher abundance of points within Type-S clusters areas, indicating a reminiscence of Type-B clusters, probably overlapped by other textures. The transformation twinning process can also be identified by the analysis of grain boundaries between magnetite-magnetite crystallites with a concentration of points near the CSL 3, CSL 9, CSL 11, CSL 27b (Cayron, 2007). These CSLs indicate twinning of magnetite ruled by the 3^n spinel law, especially the CSL 3 and 11 which are linked to our Type-B and Type-D orientation relationships respectively. Clustering near CSL 29b is also seen in Sample B grains indicating a 43.6◦ rotation about the [100] direction, related to penetration twins besides spinel law twinning. The last type of twinning was only observed in hematite of Sample II from a shallower level.

The hematite-hematite misorientation analysis, in order to identify and characterize the twinning, shows many possibilities of twinning in several directions and forms. The misorientation clusters can be divided into three distinct families: a first family which shares the rotation along [0001] direction towards c-axis, responsible for basal twinning. Two different rotations can be seen about this axis with 35° and 60°, analogues to Liebisch and Dauphiné Law on quartz respectively. A second family is identified by a single cluster along the [10-10] direction and a characteristic rotation of 75°; this cluster are related to twinning of prism sections (m-twins). A third family is spotted by two clusters along the directions [11-22] and [12-33] and with a rotation of approximately 90°, possibly related to twinning of trapezohedron forms in hematite (x-twins).

The overlapping of different crystallographic textures in martitized grains, shows that these grains possibly grew close to a source of heat. The iron (hydro)oxides minerals are susceptible to environmental changes still in solid state during the diagenesis of the pile and also the presence of intrastate percolating fluid. Such oxide-hydroxide grains function as crystallographic markers of the Archean ocean physicochemical conditions and iron formations of the region. Indirectly, the presence of these minerals can be related to the conditions of atmosphere and circulating fluids in contact with iron formations (Bekker et al. 2010, Bekker et al. 2014, Konhauser et al. 2017 and Planavsky et al. 2010).

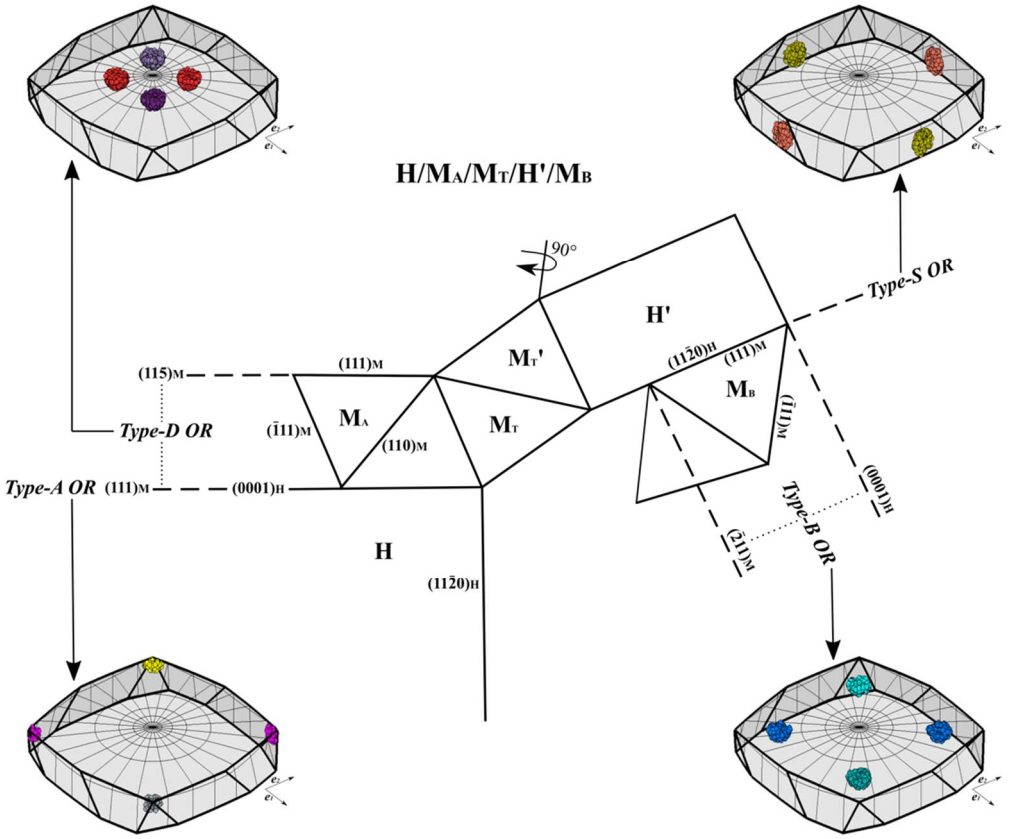

Figure 18: Projection scheme parallel to $[01\text{-}1]_M$ modified from Withers & Bursil (1980) exhibiting orientation relationships of Type-A, B, D and S for the quaternary orientationship $H/M_A/M_T/H'/M_B$ proposed, together with the expected correspondents' clusters formed into 3D-misorientation space of Axis-Angle. Note that $M_T'/H'/M_B$ should be rotated 90° diagonally in order to fit the structure theoretically, but for means of a better visualization in 2D rotation is only indicated.

The understanding of atmospheric changes in the Archean has changed and it is already considered that the transition to an oxygenated atmosphere occurred in an oscillatory manner and not abruptly as previously considered (Lyons *et al.,* 2014). Iron oxides and hydroxides are extremely susceptible to changes in terrestrial oxidation, and preserved rocks may contain remnants minerals that traces of different temperatures and oxidation/reduction conditions that occurred during the diagenesis process of iron formations.

These series of changes show that martitization is a complex process that involves: 1) topotactic transformation of magnetite into hematite, and vice versa; 2) a complex

twinning transformation system and 3) successive phase changes still in solid state during diagenesis. Such successive transformations are also responsible for a significant change in volume and in the habit of crystal due to the abrupt transformation from a crystal system of high symmetry (cubic) to symmetries of lower symmetry (trigonal and orthorhombic). Continuous and successive phase changes in elongated bands parallel to the banding show that the phase transformation continued even with the increase of the stacking pile during diagenesis.

The temperature of reduction required for generating the ORs of Type B, C and D compiled by Bursill & Whiter (1979) are not consistent with the low temperature metamorphism from the iron formation of the Serra Norte Deposits (Dalstra & Guedes, 2004 and Macambira & Schrank, 2002). There are two possibilities to explain the larger amount of phase transformation in these rocks: either there is a greater contribution in the oxidation/reductions condition due to atmospheric changes or there is a source of heat near the iron formation during diagenesis.

The orientation relationships of greatest importance in the misorientation analysis of the hematite-goethite transformation interface is Type-α, regarding the orientation $(0001)_{Hem} \parallel (001)_{Ght}$, $[11\text{-}20]_{Hem} \parallel [100]_{Ght}$, which implies in a rotation of zero degrees towards the c-axis. This is the most common and abundant texture between these two minerals and they represent the expected OR and misorientation angle necessary for a topotactic transition between the two phases conserving the oxygen lattice stacking, as expected. A second case less common, but also present in the martitized grains samples is Type-β OR regarding a similar orientation of Type-α but now with a 30^{o} rotation towards the c-axis and using first order prism direction as reference. Type-β OR is also an indicative of topotaxity and it is an expected cluster resultant from the previous and more abundant Type- α.

Type- α clusters contribute from 12.36% to 31.84% in the total of plotted points, thus being the predominant crystallographic texture between these two phases. It is verified that there is topotaxity in the phase transformation between hematite and goethite. Although the density of points is not as vast as in the previous transformation process (magnetite-hematite), Type-α clusters are the most abundant in martitized grains. The twinning process in hematite concomitant with the phase transformation to goethite, implies in other two ORs here called Type-γ and Type-δ, which contribute with 6.39% to 15.28% of the total misorientation points plotted. These ORs, with a rotation of

approximately 90º are possibly linked with x-twinning in hematite, creating these ORs between newly topotactic formed goethite and trapezohedron twins in hematite. A further analysis with higher density of points is necessary and recommended for mapping all possible ORs between transformed goethite and other possible hematite twins.

The iron oxides and hydroxides that make up the matrix of both sample show by their pole figures an expected crystallographic orientation where the crystal's *c-axis* is perpendicular to the primary rock banding and the crystals were allowed to grow along their *a* and *b-axis*. This is an expected orientation for the microplaty matrix of a non-deformed iron formation and it shows that crystals have grown and spontaneously transformed during diagenesis.

4.2. Mineral Characterization

One of the great difficulties during quantitative microscopy analyses of iron ore is to quantify and identify the multiple iron phases which compound the ore. A preliminary Mössbauer Spectroscopy analysis could be a very precise and helpful tool to identify those phases and appraise its abundance between the other iron-rich phases, as a first moment calibration of Fe-bearing minerals followed by other methods as X-Ray Diffraction with a Rietveld Refinement analysis or quantitative automated analysis of minerals by scanning electron microscopy platforms (e.g. QEMSCAN, MLA or TIMA-X).

The SiO_2 concentration has an instant increase at jaspilite levels (Fig. 14) and MgO anomalies are only observed at JP(T) and JP(C) levels due to the presence of talc and dolomite (Prado et al. 2016). The concentration of CaO is lower at JP(T) domains when compared to JP(C). This different type of impure goethite can also be seen in Mössbauer spectrum of sample F1051-04 (Fig. 15a) where goethite is represented by a single duplet and not a normal sextet as in the other samples. This difference is caused by the replacement of aluminum in the mineral structure, adsorbed phosphorus in the surface of the mineral and also by poorly crystallized/amorphous goethite with small crystallites of the same mineral(Yamashita et al. 2000, Tucek et al. 2013, Bowles et al. 2011, Nayak et al. 2011 and Murad & Schwertmann 1983). It is possible that this generation of goethite is not a direct product of transformation of phases because the initial composition of hematite does not match with the composition of goethite. It is probably a product of supergene alteration, precipitated at shallower levels near the surface (ore canga). The oxides/hydroxides which show a genetic relationship related to phase transformation

should have a similar composition, that is, in this case, a low content of Al_2O_3 and P_2O_5.

The ADS logging obtained by reflectance spectroradiometry proposed in Prado et al. (2016) (Fig. 14) and the quantitative characterization by ^{57}Fe Mössbauer seem to be in consonance. They are reasonable for characterizing the levels of ore canga and hematite friable ore, which are only composed by Fe-bearing minerals as goethite and hematite. Comparing both methods, we are able to distinguish between FH(H) and FH(HG) (Fig. 16), hematite friable ore rich in hematite and hematite/goethite respectively, confirming the efficiency of reflectance spectroradiometry in determining the modal composition of iron oxides/hydroxides. At the jaspilite levels, the Mössbauer relative concentrations does not correspond to the bulk modal mineralogy, apparently due to the presence of other minerals undistinguishable by the technique as quartz, talc and dolomite.

5. Conclusions

The data demonstrate that in martitization, the transformation of magnetite-hematite-goethite occurs in a topotactic manner and the crystallographic memory can be checked in any of the directions of the transformation reaction. The orientation relationships Type-A in the magnetite-hematite transformation and Type-α in the hematite-goethite transformation are the main ORs in the analyzed martitized grains and represent the main crystallographic texture of the banded iron formations called jaspilites of the N4WS deposit. It evidences that there is a strong crystallographic control of the phase's emplacement and that the oxygen lattice framework is preserved through the whole transformation of the three target phases of the Fe-O system.

Other high-index orientation relationships, such as Type-B, Type-C and Type-S, once identified by Heizmann (1981), Becker *et al.* (1977) and Withers & Bursil (1980) in experimental studies are here evidenced. They are not an indication of topotacticity, but a marker of a complex twinning process occurred during diagenesis and different conditions of reduction-temperature in between phase transformation. There is a visible difference between the misorientation characterization of grains and the microplate matrix, which shows a higher prevalence of high-index ORs such as Type-B, demonstrating a different dynamic of crystallographic memory than the posterior formed grains.

The martitized grains under low-grade metamorphism provides favorable conditions to preserve their crystallographic memory in different moments of phase transformation

and oxidation/reduction conditions. Often those textures are overprinted by the most common orientation relationship of topotactic transformation (Type-A) or other ORs caused by strain. The preservation of high-index orientation relationships in the grain boundaries interface and in the matrix is an evidence of progressive and dynamic cycles of oxidation-reduction and/or a nearby source of heat during the diagenesis.

The study of crystallographic textures by three-dimensional misorientation analysis of geological samples, especially iron formations, is still in the beginning but represents an excellent tool for characterization and quantification of orientation relationships related to phase transformation, twinning and deformation. It is recommended that more studies in another Archean iron formations, targeting the reaction between iron oxides/hydroxides for comparison purposes. On the other hand, we recommend the use of transmission electron microscopy for verifying grain boundary misorientation and orientation relationships *in situ* should be added to classical works to a better understanding of the main ORs listed and quantified in this paper.

During characterization of the iron ore by Mössbauer Spectroscopy, it was possible to identify the same ore facies described by semi-quantitative methods of reflectance spectroradiometry. The method is useful, especially in iron rich rocks as, for example, the Friable Hematite (FH), where the Mössbauer Spectra showed really close results to the truly modal composition of the whole rock probably due to the absence or low concentrations of quartz and other mineral phases. The method is useful to show the homogeneous aspects of the Friable Hematite (HG) ore and also to stablish a parameter to differentiate the goethite originated from phase transformation and Al- substituted and phosphorus adsorbed goethite.

5. References

Barbosa, P. F. & Lagoeiro, L. (2010). Crystallographic texture of the magnetite-hematite transformation: Evidence for topotactic relationships in natural samples from Quadrilátero Ferrífero, Brazil. American Mineralogist. 95, 118-125.

Becker, P., Heizmann, J.J. and Baro, R. (1977). Relations Topotaxiques entre des Cristaux Naturels D'Hématite et la Magnétite qui en est Isse par Réduction à Basse Température. Journal of Applied Crystallography. 10, 77-78.

Bekker, A., Slack, J., Planavsky, N., Krapež, B., Hofmann, A., Konhauser, K.O., Rouxel, O.J., 2010. Iron formation: the sedimentary product of a complex interplay among mantle, tectonic, oceanic, and biospheric processes. Econ. Geol. 105, 467–508.

Bekker, A., Planavsky, N., Krapež, B., Rasmussen, B., Hofmann, A., Slack, J.F., Rouxel, O.J., Konhauser, K.O., 2014. Iron formations: their origins and implications for ancient seawater chemistry. In: Holland, H.D., Turekian, K.K. (Eds.), Treatise of Geochemistry, second ed. v. 9. Elsevier, pp. 561–628.

Bursill, L.A. and Withers, R.L. (1979). On the Multiple Orientation Relationships between Hematite and Magnetite. Journal of Applied Crystallography. 12, 287-294

Cayron, C. (2007). Multiple twinning in cubic crystals: geometric/algebraic study and its application for the identification of the R3n grain boundaries. Acta Crystallographica. A63, pp. 11-29.

Cornell, R.M. and Schwetmann, U. (1996). The iron oxides: structure, properties, reactions, occurrences and uses. VCH, Weihnheim.

Cuennec, Y., Lecerf, A. (2005). Topotactic transformations of goethite and lepidocrocite into hematite and maghemite. In: Solid State Sciences. v7, 520-529.

Dalstra, L.W., and Guedes, S. (2004). Giant hydrothermal hematite deposits with Mg-Fe metasomatism: A comparison of the Carajás, Hamersley, and other iron ores. Economical Geology. 99, 1793–1800.

Davis, B.L. (1968). Fabric and structural characteristics of the martitization process.

American Journal of Science. 266., 482-496.

Ferreira, V. N., Silva, A. M., Toledo, C. L. B., Jácomo, M. H., Assis, L. M., Pires, A. C. B. The use of alternative methods for differentiation of banded iron formations and iron ore in the body N4WS, Serra Norte – Carajás mineral province. Revista Brasileira de Geofísica. v. 34, n. 1, 2015.

Gibbs, A.K., Wirth, K.R., Hirata, W.K., Olszewski, e, W. J., J. Age and composition of the Grão Pará Group volcanics, Serra dos Carajás. Rev. Bras. Geosci. 16, 201–211, 1986.

He, Y., Godet, S. And Jonas, J. J. (2005). Representation of misorientations in Rodrigues–Frank space: application to the Bain, Kurdjumov–Sachs, Nishiyama–Wassermann and Pitsch orientation relationships in the Gibeon meteorite. Acta Materialia. 53, 1179-1190.

Heizmann, J.J., Becker, P., and Baro, R. (1981) The influence of crystallite orientation on the chemical reactivity of hematite α-Fe2O3 and magnetite Fe3O4. Journal of Applied Crystallography. 14, 270–273.

Hielscher, R., & Schaeben, H. (2008). A novel pole figure inversion method: specification of the MTEX algorithm. Journal of Applied Crystallography, 41(6), 1024-1037.

Konhauser, K. O., Planavsky, N.J., Hardity, D.S., Robbins, L.J., Warchola, T.J., Haugaard, R., Lalonde, S.V., Partin, C.A., OonK, P.B.H., Tsiko, H., Lyon, T.W., Bekker, A., Johnson, C.M. 2017. Iron formations: A global record of Neoarchaean to Palaeoproterozoic environmental history. Earth-Science Reviews. 172, pp 140-177.

Krakow, R., Bennett, R. J, Johnstone, D.N., Vukmanovic, Z., Solano-Alvarez, W., Lainé, S. J., Einsle, J.F., Midgley, P.A., Rae, C.M.F., Hielscher, R. (2007). On three dimensional misorientations spaces. Proceedings of the Royal Society A. 473: 20170274.

Lagoeiro, L. E. (1998). Transformation of magnetite to hematite and its influence on the dissolution of iron oxide minerals. Journal of Metamorphic Geology, 16(3), 415-423.

Lyons, T.W., Reinhard, C.T. and Planavsky, N.J. (2014). The rise of oxygen in Earth's early ocean and atmosphere. Nature. 506, 307-315.

Macambira, J.B. O Ambiente Deposicional Da Formação Carajás e Uma Proposta de Modelo Evolutivo Para a Bacia Grão-Pará. Instituto de Geociências, Universidade Estadual de Campinas, Tese de Doutorado (217 p.), 2003.

Macambira, J.B., Schrank, A. (2002). Químio-estratigrafia e evolução dos jaspilitos da Formação Carajás (PA). Revista Brasileira de Geociências. 32, 567–578.

Machado, N., Lindenmayer, Z., Krogh, T.E., e Lindenmayer, D. UPb geochronology of Archean magmatism and basement reactivation in the Carajás area, Amazon shield, Brazil. Precambrian Res. 49, 329–354, 1991.

Martins, P. L. G., Toledo, C. L. B., Silva, A. M., Chemale Jr., F., Santos, J. O. S., Assis, L. M. Neoarchean magmatism in the southeastern Amazonian Craton, Brazil: Petrography, geochemistry and tectonic significance of basalts from the Carajás Basin. Precambrian Res. 302, 340–357, 2017.

Modaressi, A., El Abdouni, H. and Heizmann, J.J. (1989). Three new orientations of the magnetite observed during the reduction of hematite between 700-800ºC and explanation of the multiplicity of the different orientation. Reavtivity of Solids. 7, 19-27.

Murad, E. and Schwertmann, U. (1983). The Influence of Aluminium Substitution and Crystallinity on the Mössbauer Spectra of Goethite. Clay Mineral. 18, 301-312.

Nayak, P.K., Das, D., Vijayan, V., Singh, P., Chakravortty, V. (2001) 57Fe Mössbauer and EDXRF studies on three representative banded iron formations (BIFs) of Orissa, India. Nuclear Instruments and Methods in Physics Research B. 184, 649-654.

Partiti, C. S. M. Espectroscopia Mössbauer na Análise de Óxidos e Hidróxidos de Ferro. Instituto de Física da Universidade de São Paulo, 2006.

Planavsky, N., Bekker, A., Rouxel, O. J., Kamber, B., Hofmann, A., Knudsen, A., Lyons, T. W. (2010). Rare Earth Element and yttrium compositions of Archean and Paleoproterozoic Fe formations revisited: New perspectives on the significance and mechanisms of deposition. Geochimica et Cosmochimica Acta. 74-22, 6387-6405.

Prado, E. M. G., Silva, A. M., Ducart, D. F., Toledo, C. L. B., Assis, L. M. Reflectance spectroradiometry applied to a semi-quantitative analysis of the mineralogy of the N4ws

deposit, Carajás Mineral Province, Pará, Brazil. Ore Geology Reviews. v. 78, p. 101-119, 2016.

Tuček, J.; Machala, J.; Frydrych, J.; Pechoušek, J.; Zbořil, R.; Mössbauer Spectroscopy in Study of Nanocrystalline Iron Oxides from Thermal Processes. In: Mössbauer Spectroscopy: Applications in Chemistry, Biology, and Nanotechnology, First Edition. John Wiley & Sons, Inc. Published 2013

Vasquez, M.L., Carvalho, J. M. A., Sousa, C.S., Ricci, P.S.F., Macambira, E. M. B., Costa, L.T. R. Mapa Geológico do Pará em SIG. Brazilian Geological Survey – CPRM, 2005.

Withers, R.L and Bursill, L.A. (1980). High-Order Structural Relationships Between Hematite and Magnetite. Journal of Applied Crystallography. 93, 346-353.

Yamashita, M., Misawa, T., Balasubramanian, R. and Cook, D.C. (2000). Mössbauer Spectrocopic Study on X-ray Amorphous Substance in Rust Layer of Weathering Steel Subjected to Long-Term Exposure in North America. Zairyo-to-Kankyo. 49, 82-87.

Acknowledgments

The authors thank the Potsdam Imaging and Spectral Analysis (PISA) Facility of the German Research Centre for Geosciences (GFZ) for the scanning electron microscope facilities and EBSD analysis, The Center of Microscopy of the Federal University of Minas Gerais (UFMG) for the sample preparation and the colloidal silica polishing and The Center of Electron Microscopy (CME) of the Federal University of Paraná for the help in using the software for EBSD processing. The financial support of the Helmholtz Recruiting Initiative (grant No. I-044-16-01) is acknowledged.